The Integrated Sachs-Wolfe Effect with Planck and the 2MASS Photometric Redshift Catalogue

Louise Steward

September 2014

A project submitted in partial fulfilment of the requirements for the degree M.Sc. in the Department of Astronomy, as part of the National Astrophysics and Space Science Programme
UNIVERSITY OF CAPE TOWN

Supervisors: Prof T. Jarrett and Dr. M. Bilicki

Abstract

This thesis presents a measurement of the Integrated Sachs-Wolfe (ISW) effect through cross-correlation of the Cosmic Microwave Background (CMB) and the galaxy distribution tracing the large scale structure of the Universe. The CMB data used are from the 2013 release from the Planck satellite, and the large-scale structure data are from the 2MASS Photometric Redshift Catalogue (2MPZ). The galaxy data were divided into redshift shells, and `HEALPix` was used to create pixelised maps of the CMB temperature anisotropies and the galaxy overdensity. The linear galaxy bias, relating the galaxy density distribution to the underlying matter density distribution, was measured through least squares fitting of the theoretical prediction of the galaxy auto-correlation function in each redshift shell.The bias values were then used to rescale the theoretical predictions for the matter-CMB cross-correlation functions in each shell. The observed cross-correlation function between the Planck and 2MPZ data in each shell was computed, and the uncertainties associated with each measurement were calculated using cross-correlation of simulated CMB and galaxy overdensity maps. To quantify the possible detection of the ISW effect, hypothesis testing was performed through computation of the covariance matrix and χ^2 statistic in each shell. Detection of the ISW effect was found to be preferred over no detection in every case, with a total likelihood ratio of 3.4:1. While this is not quite strong evidence of detection of the ISW effect, this ratio is more than twice better than previous measurements using photometric redshift shells. While the photometric redshifts in the 2MPZ are more accurate than those that have been used before, a strong detection is out of reach with this data, as the redshifts in the 2MPZ are too shallow for more decisive ISW detection.

Acknowledgements

First and foremost, I must thank Prof. Tom Jarrett and Dr. Maciek Bilicki for their tireless effort in the supervision of my research. You have spent countless hours answering all of my many questions and encouraging me to achieve the most from my work, and your dedication to and love for the field have been an inspiration.

I would also like to thank Dr. Michelle Cluver for all of the support she has given me, both scientifically and emotionally. Without your constant encouragement and friendship the completion of this thesis would not have been possible.

Thanks to Prof. John Peacock for the advice and resources provided during your visit to Cape Town, and thanks to Dr. David Alonso for the kind use of your galaxy mock catalogues.

Finally, my deepest thanks to my family and friends for your support during the course of this thesis, for patiently listening to me talk (at length) about my work and for encouraging me every step of the way. Mom and Dad, you have given me every opportunity I could ever have dreamed of, and I wouldn't be where I am today without you.

Plagiarism Declaration

I, Louise Steward, know the meaning of plagiarism and declare that all of the work in this document, save for that which is properly acknowledged, is my own.

Contents

List of Figures

List of Tables

Chapter 1

Introduction

The cosmic microwave background (CMB) radiation is one of the most powerful tools scientists have for exploring the formation and evolution of the Universe. Not only does it contain information about the Universe as it was roughly 300 000 years after the Big Bang, the furthest back in time that can be explored without a neutrino or gravitational wave background, but it can also tell us about what things are like closer to home. The late-time integrated Sachs-Wolfe (ISW) effect is one such example of how the CMB can be used to explore the nearby Universe.

1.1 Background

The integrated Sachs-Wolfe effect (Sachs & Wolfe 1967) is a secondary anisotropy in the CMB radiation. The primary anisotropies are due to effects which occurred at or before the surface of last scattering. Secondary anisotropies are then photon energy fluctuations that have occurred since that time.

In their original paper on the topic, R. K. Sachs and A. M. Wolfe predicted the existence of an anisotropy in the CMB caused by gravitational redshift, and it was the first paper to predict an anisotropy in what was then thought to be a smooth photon energy field. Through integration of the geodesic equation in a perturbed Friedmann-Robertson-Walker metric, they predicted a fluctuation in the photon energies as the light rays travelled through the gravitational potential fields of structures in the Universe.

Then, with the advent of the ΛCDM cosmological model – that of a Universe containing cold dark matter as well as a cosmological constant Λ – Crittenden & Turok (1996) realised that a decay in the gravitational potential field in the Λ-dominated Universe at $z < 1$ could produce an ISW signal. They also laid out a framework for the measurement of the ISW effect through cross-correlation of a tracer of the large-scale structure with the CMB temperature anisotropies.

Measurement of the ISW effect therefore represents an independent detection of Dark Energy in the Universe. CMB photons travelling through space pass through the gravitational potential wells of the large-scale structure. As the photons fall into a potential well they gain energy and are blueshifted, and as they climb out they are redshifted. In an Einstein-de Sitter universe, these effects cancel out and no net change in the photon energies is observed on the large scale. However, in an open, flat universe dominated by Dark Energy, the overall decay of the gravitational potential wells causes a net overall effect, with additional blueshifting caused by clusters of galaxies and redshifting caused by voids.

The temperature fluctuations brought about by the ISW effect can be calculated using

$$\frac{\Delta T^{\mathrm{ISW}}}{T_{\mathrm{CMB}}} = 2 \int_{t_{\mathrm{LS}}}^{t_0} \frac{\dot{\Phi}\left(\vec{x}(t), t\right)}{c^2} \, \mathrm{d}t \tag{1.1}$$

where T is the temperature, t_0 and t_{LS} are the times today and at last scattering respectively, $\vec{x}$ is the position along the line of sight of the photon at time t and Φ is the gravitational potential.

The anisotropies brought about as a result of the ISW effect are subdominant to the primary CMB anisotropies, making it almost impossible to detect through direct measurement. Instead, the method of cross-correlation of the CMB with tracers of the large-scale structure is used, so that large hot spots in the CMB should correspond to overdense regions in the galaxy distribution.

In order to perform this cross-correlation, information about the galaxy distribution in the nearby Universe is needed. These data need to cover as large a fraction of the sky as possible – the cross-correlation function is inversely proportional to the area of the sky common to both the CMB and galaxy data (Afshordi et al. 2004) – and need to extend as far in terms of redshift as possible – the strength of a detection of the ISW effect increases with increasing redshift (Francis & Peacock 2010). The redshift values also need to be accurate – the theoretical prediction of the cross-correlation function relies on the redshift distribution of the galaxies used to trace the large-scale structure, so an incorrectly estimated redshift distribution will lead to incorrect predictions.

A photometric redshift catalogue such as the one used in this work is therefore ideal for measurement of the ISW effect. As the catalogue is based on all-sky photometric surveys, the sky coverage is greater than that of any one spectroscopic redshift catalogue. The accuracy of the redshifts obtained ensures a well-estimated redshift distribution, and the relative completeness of the catalogue ensures suppression of shot noise even out to $z \sim 0.3$.

Shot noise, better known as Poisson noise, is an additional uncertainty in the cross-

correlation brought about due to the discrete sampling of the underlying density field by the observation of galaxies (Dekel & Lahav 1999). The local galaxy density field is a continuous function, which galaxy surveys aim to recover using observations. A galaxy is a discrete object which is assumed to have been Poisson sampled from the underlying density field. The use of galaxies in the reconstruction of the density field will therefore introduce shot noise into the recovered field. The more galaxies that are sampled, the lower the shot noise will be.

Whilst galaxies are used as a tracer of the large-scale structure of the Universe, the structure itself is comprised mostly of Dark Matter. A relationship between the galaxy density field and the matter density field therefore needs to be established, so that the overall matter density field can be used to predict the ISW effect. A linear galaxy bias is used here, with $\delta_g = b\delta_m$, where δ_g and δ_m are the galaxy and matter overdensity fields respectively.

Unfortunately, no galaxy survey is perfect. Galaxy observations are nearly impossible in certain regions of the sky – the Zone of Avoidance, where dust and stars in the Milky Way hinder observations, as well as regions such as the Magellanic Clouds – and the incomplete sky coverage leads to a loss of power in the angular power spectrum of the galaxy distribution. A similar problem arises with observations of the CMB – emission from the Milky Way as well as from nearby microwave point sources prevent observation of the surface of last scattering over the whole sky. The loss of power in the angular power spectra can be corrected for, at first approximation, by multiplying the power spectrum by the inverse of the square root of the fraction of the sky that contains reliable information about the temperature or density distribution – the initial power spectrum is multiplied by the appropriate factor of $1/\sqrt{f_{\rm sky}}$ to compensate for the fact that the coverage is not the full 4π sr of the sky. (Rassat et al. 2007)

1.2 Mathematical Framework

In this work, the ISW effect will be examined through cross-correlation of the CMB temperature anisotropies with galaxy distribution data as a tracer of large-scale structure. Here follows a summary of the mathematical framework required for the prediction of the ISW effect as it manifests in the CMB-galaxy cross-correlation function, following that given in Francis & Peacock (2010). A full derivation of the theoretical predictions for the auto- and cross-correlation functions can be seen in the Appendix.

The cross-correlation between the galaxy overdensity field and the CMB temperature field is given by

$$\langle a^{\rm g}_{\ell m} a^{{\rm T}*}_{\ell' m'} \rangle = C_{\rm gT}(\ell)\ \delta^{\rm K}_{\ell\ell'} \delta^{\rm K}_{mm'} \tag{1.2}$$

where $a^{\rm g}_{\ell m}$ and $a^{\rm T}_{\ell m}$ are the spherical harmonic coefficients for the galaxy overdensity and temperature fields respectively, and $\delta^{\rm K}$ is the Kronecker delta.

Poisson's equation, in Fourier space and within the linear regime, relates the time derivative of the gravitational potential field to the matter density field

$$k^2\ \dot{\Phi}_k = \frac{-3\ H_0^2\ \Omega_m}{2} \frac{\mathrm{d}}{\mathrm{d}t}\left[\frac{g(a)}{a}\right] \delta_k(z=0) \tag{1.3}$$

where $a = (1+z)^{-1}$ is the scale factor, $g(a)$ is the linear growth factor, normalised so that $g(0) = 1$, δ_k is the overdensity field defined as $\delta = \rho/\langle\rho\rangle - 1$, and $H_0 = 100h$ is the Hubble constant. Table 1.1 shows the best-fit cosmological parameters used for the theoretical predictions. From Equation 1.1, it can then be seen that

$$\begin{aligned} \frac{a^{\rm T}_{\ell m}}{T} &= \frac{-3H_0^2\ \Omega_m}{(2\pi)^3\ c^3} \int \mathrm{d}\Omega\ Y^*_{\ell m}(\hat{\mathbf{n}}) \int \mathrm{d}r\ a\ \frac{\mathrm{d}}{\mathrm{d}t}\left[\frac{g}{a}\right] \int \frac{\mathrm{d}\mathbf{k}}{k^2}\ \delta_k\ e^{i\mathbf{k}\cdot\hat{\mathbf{n}}r} \\ &= \frac{-3H_0^2\ \Omega_m\ i^\ell}{2\pi^2 c^3} \int \mathrm{d}r\ a\ \frac{\mathrm{d}}{\mathrm{d}t}\left[\frac{g}{a}\right] \int \frac{\mathrm{d}^3\mathbf{k}}{k^2}\ \delta_k\ j_\ell(kr)\ Y^*_{\ell m}(\hat{\mathbf{k}}) \end{aligned} \tag{1.4}$$

where δ is the matter overdensity field today, $\hat{\mathbf{k}}$ and $\hat{\mathbf{n}}$ are unit vectors and the exponential term has been expressed in terms of the spherical Bessel functions of the first kind j_ℓ and the spherical harmonics $Y_{\ell m}$.

The projected galaxy overdensity $\delta_{\rm proj}$ is related to the three-dimensional galaxy overdensity by

$$\begin{aligned} \delta_{\rm proj} &= \int \frac{\bar{n}(r)\ r^2}{\int \bar{n}(r')\ r'^2\ \mathrm{d}r'} \delta(r)\ \mathrm{d}r \\ &\equiv \int \Theta(r)\ \delta(r)\ \mathrm{d}r \end{aligned} \tag{1.5}$$

where $\bar{n}(r)$ is the background galaxy number density and $r(z)$ is the comoving distance. $\Theta(r)$ is therefore the effective radial weight applied to the density field, which will depend on the redshift distribution of the galaxy sample.

Having assumed a linear bias relation of the galaxy and matter overdensity fields $\delta_{\rm g} = b\delta_{\rm m}$, the galaxy coefficients can be expressed as

$$a^{\rm g}_{\ell m} = \frac{bi^\ell}{2\pi^2} \int \mathrm{d}r\ g\ \Theta(r) \int \mathrm{d}^3\mathbf{k}\ \delta_k\ j_\ell(kr)\ Y_{\ell m}(\hat{\mathbf{k}}) \tag{1.6}$$

where δ is again the matter overdensity today and $\hat{\mathbf{k}}$ is a unit vector.

Substitution then gives the cross-correlation as

$$C_{\rm gT}(\ell) = \frac{-6b\ H_0^2\ \Omega_m\ T}{\pi c^3} \int {\rm d}k\ P(k) \int {\rm d}r'\ g\ \Theta(r')\ j_\ell(kr') \int {\rm d}r\ g\ H(f-1)\ j_\ell(kr) \quad (1.7)$$

where $f(z)$ is the growth function, related to $g(z)$ by $f = {\rm d}\ln g/{\rm d}\ln a$, and, in the flat case where $\Omega_m + \Omega_\Lambda = 1$, $H(z) = H_0 E(z) = H_0[\Omega_m(1+z)^3 + (1-\Omega_m)]^{1/2}$.

The spherical Bessel functions can be removed for computational simplicity using Limber's approximation in the small angle limit

$$\lim_{\ell\to\infty} j_\ell(x) = \sqrt{\frac{\pi}{2\ell+1}}\ \delta^{\rm K}(\ell + 1/2 - x) \quad (1.8)$$

This approximation, while not exact at large angles, gives a solution which only differs from the exact solution by around 10% for $\ell \lesssim 10$, and in this case, observational errors will far outweigh this effect (Rassat et al. 2007). When this is applied to Equation 1.7, it gives

$$C_{\rm gT}(\ell) = \frac{-3b\ H_0^2\ \Omega_m\ T}{c^3\ (\ell+1/2)^2} \int {\rm d}r\ \Theta(r)\ H\ g^2\ (f-1)\ P\left(\frac{\ell+1/2}{r}\right) \quad (1.9)$$

Following the same method, the galaxy auto-correlation function is found to be

$$C_{\rm gg}(\ell) = \frac{2b^2}{\pi} \int {\rm d}k\ k^2\ P(k) \left| \int {\rm d}r\ g\ \Theta(r)\ j_\ell(kr) \right|^2 \quad (1.10)$$

and applying the Limber approximation (Kaiser 1992)

$$C_{\rm gg}(\ell) = b^2 \int {\rm d}r\ \frac{\Theta^2}{r^2}\ g^2\ P\left(\frac{\ell+1/2}{r}\right) \quad (1.11)$$

Both Equation 1.9 and Equation 1.11 contain terms dependent on both r and z. For ease of computation, these equations are re-expressed in terms of z only (see Appendix) to finally give

$$C_{\rm gT}(\ell) = \frac{-3b\ H_0^2\ \Omega_m\ T}{c^3(\ell+1/2)^2} \int {\rm d}z\ \theta(z)\ E(z)\ (f-1)\ g^2\ P\left(\frac{\ell+1/2}{r(z)}\right) \quad (1.12)$$

and

$$C_{\rm gg}(\ell) = b^2 \frac{H_0^3}{c^3} \int {\rm d}z\ \frac{\theta(z)^2\ E(z)}{(\int_0^z {\rm d}x/E(x))^2}\ g^2\ P\left(\frac{\ell+1/2}{r(z)}\right) \quad (1.13)$$

where

$$\theta(z)\ {\rm d}z = \Theta(r)\ {\rm d}r \quad (1.14)$$

$$= \frac{\mathcal{N}(z)}{\int {\rm d}x\ \mathcal{N}(x)} \quad (1.15)$$

with $\mathcal{N}(z)$ the redshift distribution in each redshift shell.

Table 1.1: A summary of the best-fit cosmological parameters obtained from the Planck survey (Planck Collaboration et al. 2013a).

Parameter	Value	Definition
t_0	13.819	Age of the Universe today (Gyr)
H_0	67.11	Current expansion rate (km s^{-1} Mpc^{-1})
$\Omega_\mathrm{b}h^2$	0.022068	Baryon density today
$\Omega_\mathrm{c}h^2$	0.12029	Cold dark matter density today
Ω_Λ	0.6825	Dark energy density divided by critical density today
σ_8	0.8344	RMS matter fluctuations today in linear theory
n_s	0.9624	Scalar spectrum power law index
τ	0.0925	Thomson scatter optical depth due to reionisation

1.3 The ISW Effect So Far

Figure 1.1, a table reproduced from Nishizawa (2014), shows the results of ISW studies so far. It can be seen that over the years, a number of authors have used different data and methods to attempt to detect the ISW effect.

It will be useful to compare the results of this work with those acquired by other authors, especially those authors who have used similar data and methods.

The results of the authors whose galaxy density data are derived from 2MASS will be of particular interest, as the data used in this work are based on 2MASS. The newly created 2MASS Photometric Redshift catalogue is used for the galaxy distribution data (see Section 2.4). Whilst it would be preferable to use a deeper data set such as WISE for this analysis, neither a resolved extended source catalogue nor a photometric redshift catalogue yet exist for this survey. Unfortunately, other than Francis & Peacock (2010), upon whose method this work is based, no other works have made use of redshift shells in the creation of galaxy overdensity maps, as photometric redshifts were not yet available for 2MASS. This makes it difficult to draw a direct comparison between these previous results and the result of this work (see Section 5.2).

The first ISW measurement attempted using 2MASS was made by Afshordi et al. (2004), correlating the galaxy overdensity with the WMAP1 CMB temperature maps. They split the 2MASS XSC data into magnitude bins rather then redshift shells, inferring the redshift distribution in each bin from the Schechter (1976) parameters fit to the K_S-band luminosity function. The redshift distribution can be expressed in terms of the luminosity function as

$$\frac{\mathrm{d}N}{\mathrm{d}z}(z)\,\mathrm{d}z = \int_{M_b(z)}^{M_f(z)} \Phi(M)\,\mathrm{d}M \times \frac{\mathrm{d}V_c}{\mathrm{d}z}\,\mathrm{d}z \tag{1.16}$$

where $\mathrm{d}V_c/\mathrm{d}z$ is the line-of-sight comoving volume element and

$$\begin{aligned} M_f(z) &\equiv m_{\text{faint}} - DM(z) - k(z) \\ M_b(z) &\equiv m_{\text{bright}} - DM(z) - k(z) \end{aligned}$$

with $DM(z)$ and $k(z)$ are the distance modulus and k-correction at redshift z respectively.

This derived redshift distribution, which spanned in total between $0.0 < z < 0.2$, was then used for the theoretical predictions of the auto- and cross-correlation functions. They were able to detect the ISW effect at the 2.5σ level, and set the precedent for future ISW work with 2MASS.

This same method of estimating the redshift distribution for the 2MASS galaxies in bins of K_S-band magnitude was used by Rassat et al. (2007) and Ho et al. (2008), where the correlation was performed with the WMAP 3 data in both cases.

Ho et al. (2008) used the 2MASS data as part of a larger galaxy data set utilising distribution information from surveys in the infrared, optical and radio regimes. Rassat et al. (2007) used only the 2MASS data for the overdensity analysis, updating the work done by Afshordi et al. (2004). Neither Rassat et al. (2007) nor Ho et al. (2008) detected the ISW effect above the 1.5σ level with 2MASS.

The other approach to the detection of the ISW effect with 2MASS in the absence of photometric redshifts is the estimation of the redshift distribution for the entire catalogue at once. This approach was taken by both Gaztañaga et al. (2006) and Giannantonio et al. (2008), (2012). Both teams made use of WMAP3 CMB data, with Giannantonio et al. (2012) later updating their work with the WMAP7 data release. Once again, neither team were able to make a detection at greater then a 1.4σ level, with the majority of the results falling short of the 1σ level.

None of the ISW measurements with 2MASS after Afshordi et al. (2004) have produced a statistically significant result – it is the intention of this work to use accurate photometric redshifts and new CMB data to ameliorate this.

Author	CMB	LSS data	Redshift	Method	Detection	DE Constraints
Kneissl et al. '97	COBE4	ROSAT XRB	N/A	CCF	No detection	–
Boughn & Crittenden '98	COBE4	HEAO1 XRB	$z \simeq 1$	CCF	No detection	–
Boughn & Crittenden '02	COBE4	NVSS	$0 < z < 2$	CCF	No detection	$\Omega_\Lambda < 0.74$
Boughn & Crittenden '04,'05	WMAP1	NVSS/HEAO1 XRB	$0 < z < 2$	CCF	2-3σ	–
Fosalba & Gaztanaga '04	WMAP1	APM	$z \simeq 0.15$	CCF	2.5σ	$\Omega_\Lambda = 0.8^{+0.06}_{-0.27}(2\sigma)$
Fosalba et al. '03	WMAP1	SDSS1(main, LRG)	$z \simeq 0.3, 0.5$	CCF	$2.0, 3.0\sigma$	–
		combined			3.6σ	$\Omega_\Lambda = 0.8^{+0.06}_{-0.11}(2\sigma)$
Scranton et al. '03	WMAP1	SDSS1(LRG)	$0.3 < z_p < 0.8$	CCF	$> 2\sigma$	–
Nolta et al. '04	WMAP1	NVSS	$0 < z < 2$	CCF	2.6σ	$\Omega_\Lambda = 0.68_{-0.68}(2.2\sigma)$
Afshordi et al. '04	WMAP1	2MASS	$0 < z < 0.2$	APS	2.5σ	–
Padmanabhan et al. '05	WMAP1	SDSS4(LRG)	$0.2 < z_p < 0.6$	APS	2.5σ	$\Omega_\Lambda = 0.8^{+0.05}_{-0.19}(2\sigma)$
Gaztanaga et al. '06	WMAP1	2MASS	$z \sim 0.1$	CCF	4σ	$\Omega_\Lambda = 0.70^{\pm 0.05}(1\sigma)$[a]
		APM	$z \sim 0.15$			$w = -1.02^{\pm 0.17}(1\sigma)$[a]
		SDSS1(main,LRG)	$z \sim 0.3, 0.5$			
		NVSS+HEAO	$z \sim 0.9$			
Cabre et al. '06	WMAP3	SDSS4(main, LRG)	$z \sim 0.3, 0.5$	CCF	4.4σ	$\Omega_\Lambda \simeq 0.83$
Giannantonio et al. '06	WMAP3	SDSS4(QSO)	$0.1 < z_p < 2.7$	CCF	$2 - 2.5\sigma$	$0.075 < \Omega_m < 0.475(1\sigma)$
						$-1.18 < w < -0.76(1\sigma)$
Pietrobon et al. '06	WMAP3	NVSS	$0 < z < 2$	WLT	2.7σ	$0.41 < \Omega_\Lambda < 0.79(2\sigma)$
Vielva et al. '06	WMAP1	NVSS	$0 < z < 2$	WLT	3.3σ	$\Omega_\Lambda = 0.65^{+0.17}_{-0.20}(1\sigma)$
						$w = -0.70^{+0.35}_{-0.50}(1\sigma)$
Rassat et al. '07	WMAP3	2MASS XSC	$0 < z < 0.2$	APS	$< 1\sigma$	$\Omega_\Lambda = 0.85^{+0.04}(2\sigma)$
McEwen et al. '07	WMAP1	NVSS	$0 < z < 2$	WLT	3.9σ[b]	$\Omega_\Lambda = 0.63^{+0.18}_{-0.17}(1\sigma)$
						$w = -0.77^{+0.35}_{-0.36}(1\sigma)$
Giannantonio et al. '08, '12	WMAP3,7	2MASS	$z \sim 0.2$	CCF	$0.5\sigma, 0.7\sigma$	
		SDSS6,8(main)	$z \simeq 0.3$		$2.2\sigma, 2.2\sigma$	
		SDSS6,7(LRG)	$z \simeq 0.5$		$2.2\sigma, 2.5\sigma$	
		SDSS6(QSO)	$0 < z < 3$		$2.5\sigma, 2.3\sigma$	
		NVSS	$0 < z < 2$		$3.3\sigma, 2.8\sigma$	
		HEAO	$0 < z < 2$		$2.7\sigma, 2.4\sigma$	
		combined			$4.5\sigma, 4.4\sigma$	$\Omega_m = 0.20^{+0.19}_{-0.11}(2\sigma)$
Raccanelli et al. '08	WMAP3	NVSS	$0 < z < 2$	CCF	2.5σ	–
McEwen et al. '08	WMAP3	NVSS	$0 < z < 2$	WLT	$\sim 3\sigma$	–
Ho et al. '08	WMAP3	2MASS	$0 < z < 0.2$	CCF	$0.2 - 1.4\sigma$	
		SDSS(LRG)	$0.2 < z_p < 0.6$		$1.3 - 2.5\sigma$	
		SDSS(QSO)	$0.5 < z < 2$		$0.2 - 1.4\sigma$	
		NVSS	$0 < z < 3$		2.9σ	
		combined			3.7σ	$\Omega_\Lambda = 0.746^{\pm 0.09}(1\sigma)$
Granett et al. '08	WMAP5	SDSS6(LRG)	$0.4 < z_p < 0.75$	STK	4.4σ	–
Xia et al. '09	WMAP5	SDSS6(QSO)	$0 < z_p < 3$	CCF	$1.5 - 2.7\sigma$	$\Omega_m = 0.273^{\pm 0.019}(1\sigma)$[c]
Hernandez-Monteagudo '10	WMAP5	NVSS	$0 < z < 3$	C/A	$\sim 2 - 3\sigma$	–
Sawangwit et al. '10	WMAP5	SDSS5 (LRG)	$0.2 < z_s < 0.5$	CCF	0.8σ	–
		2SLAQ (LRG)	$0.4 < z_s < 0.7$		1.6σ	–
		AAO (LRG)	$0.5 < z_s < 0.9$		0.4σ	–
		NVSS	$0 < z < 2$		$\sim 2\sigma$	–
Lopez-Corredoira et al. '10	WMAP5	SDSS7		CCF	No detection	–
Francis & Peacock '10	WMAP3	2MASS XSC	$0 < z_p < 0.3$	APS	$\sim 1\sigma$	–
Goto et al. '12	WMAP7	WISE pre.	$0 < z < 0.3$	APS	$\sim 3\sigma$	–
Flender et al. '13	WMAP5	SDSS6 (LRG)	$0.4 < z_p < 0.75$	STK	$> 3\sigma$	–
Planck et al. XIX '13	Planck1	BOSS8[d]	$0 < z_s < 0.7$	C/A/W	1.7σ	–
		SDSS8(main)	$0.1 < z_p < 0.9$		2.0σ	–
		NVSS	$0 < z < 2$		2.9σ	–
Ilic et al. '13	WMAP7	SDSS6,7(Void)	$0 < z_s < 0.7$	STK	$\sim 3\sigma$	–
Hernandez-Monteagudo et al. '14	WMAP9	BOSS8[d]	$0.15 < z_p < 0.7$	C/A/W	$1.62 - 1.67\sigma$	
Kovacs et al. '14	WMAP7	WISE full	$z \sim 0.15$	APS	$\sim 1.0\sigma$	–
Ferraro et al. '14	WMAP9	WISE full (gal)	$z \sim 0.3$	APS	$\sim 2.6\sigma$	–
		WISE full (AGN)	$z \sim 1.1$		$\sim 1.2\sigma$	–

Figure 1.1: This table has been reproduced from Nishizawa (2014), and shows a summary of previous ISW work. It can be seen that over the years, groups with different data and different approaches have had varying degrees of success in detecting the ISW effect. Of particular interest here are the results obtained by teams using 2MASS as the source of the galaxy overdensity data. It can be seen that measurement of the ISW effect can be used to constrain both the matter and dark energy parameters of the Universe. The methods used include measurement of the angular power spectrum (APS) as well as the cross-correlation function (CCF).

1.4 Thesis Outline

The remainder of this thesis shall progress as follows: Chapter 2 describes the data used, as well as how the data were prepared for correlation analysis. Chapter 3 contains details about shot noise removal, as well as the results of the auto- and cross-correlation procedures. Chapter 4 presents the results of the analysis and the hypothesis testing. Chapter 5 discusses the results, and compares them to work by other groups. Chapter 6 concludes the thesis, and describes plans for future work.

Chapter 2

Data Preparation and Analysis

This chapter presents the tools and data used for the ISW measurement. Details of the software package used are followed by a description of the Planck CMB data and how the CMB maps are masked. The galaxy distribution catalogue is then introduced, and the methods for preparation and masking of galaxy overdensity maps are described.

2.1 HEALPix

The primary software package used for the analysis is `healpy`, a `python` wrapper of the `HEALPix` package.

In this work, `healpy` has been used for all pixelisation, resolution downgrading, smoothing, computation of spherical harmonics and auto- and cross-correlation. The all-sky maps produced using `healpy` are presented in Mollweide projection, in Galactic coordinates with the Galactic Centre at the centre of each map.

`HEALPix`* (Górski et al. 2005) – the Hierarchical Equal Area isoLatitude Pixelization – was released to the public in 1997 as a tool for the pixelisation and analysis of all-sky datasets, and was originally designed with all-sky CMB maps in mind. Its three main characteristics - hierarchical structure, equal area of pixels and isolatitude distribution of discrete area elements - ensure that it can perform, among other functions, fast and efficient spherical harmonic transforms and analysis.

A resolution parameter of `NSIDE` = 64 has been used for all of the maps unless otherwise stated. This results in 49 152 pixels each of area 0.83 deg^2 over the sky. This resolution is sufficient for ISW analysis, as the contribution of the ISW signal is only important at large scales (Planck Collaboration et al. 2013c), and a lower resolution optimises computing time. This resolution is also the most appropriate for the galaxy data, as the mean source density

*http://healpix.jpl.nasa.gov

is low (< 30 galaxies per deg^2). More details on the `HEALPix` resolution conventions can be found in Górski et al. (2005), specifically in their Table 1.

2.2 Planck CMB Data

The CMB anisotropy maps used for this analysis are from the first data release of the Planck mission* (Planck Collaboration et al. 2013a). Amongst the data products available to the public are four foreground-cleaned CMB maps, derived using different component separation algorithms (Planck Collaboration et al. 2013b). All four of these maps have been used in this work.

In previous ISW analyses using WMAP data, e.g. Francis & Peacock 2010, individual foreground-corrected frequency maps of the CMB were often used separately and cross-correlated with galaxy data. This was useful for ISW detection as this signal is expected to be achromatic (Rassat et al. 2007). In the case of the new Planck data, however, clean frequency maps are not yet available. Instead, all four of the CMB maps used in this analysis are combined maps using all of the observed Planck frequencies. This will not allow for testing of the achromatic nature of the ISW signal, but will help to verify whether any of the maps have significant systematics.

The four component separation methods are:

- C-R: The `Commander` method (Eriksen et al. 2006) models foregrounds using Bayesian parameter estimation techniques to fit a parametric signal model of the CMB to each pixel. This is combined with the `Ruler` method (Planck Collaboration et al. 2013b), using the resulting low-resolution spectral parameter maps to produce full-resolution data through foreground amplitude maximisation.
- NILC: This method is based upon the minimisation of the variance of the CMB. This is done by implementing a needlet version of the internal linear combination (ILC) algorithm (Delabrouille et al. 2009).
- SEVEM: Spectral Emission Via Expectation Maximisation (Fernández-Cobos et al. 2012) uses foreground templates constructed from the highest and lowest frequency bands to subtract foreground contamination from the main CMB bands.
- SMICA: Spectral Matching Independent Component Analysis (Cardoso et al. 2008) uses a CMB-oriented parametric approach to fit the amplitude and spectral parameters of the CMB in the harmonic domain.

FITS files containing the maps as well as the corresponding Galactic emission mask (see Section 2.3) were downloaded, and the maps were downgraded to have a resolution of 0.83 deg^2 per pixel, to match that of the galaxy data (see Section 2.6).

*http://planck.ipac.caltech.edu/

2.3 Masking of CMB Maps

Following the ISW work of the Planck Collaboration et al. (2013c), the CMB anisotropy maps were masked using their U73 mask. This is the official mask designed by the team, which excludes all regions with large Galactic and point-source contamination (Planck Collaboration et al. 2013b). This mask, like the maps mentioned in Section 2.2, was made available at the full Planck resolution of `NSIDE` = 2048, and needed to be downgraded to `NSIDE` = 64 to match the rest of the maps.

The mask was initially presented as a binary map across the whole sky: pixels with a value of 0 are regarded as part of the mask and those with a value of 1 are usable regions of the sky. Following the method presented by the Planck team in their ISW paper (Planck Collaboration et al. 2013c), the downgrading procedure then continued as follows: the binary mask was smoothed with a Gaussian kernel of FWHM three times the size of the original pixels (here approximately 5.72′). This smoothed mask was then downgraded to a resolution of `NSIDE` = 64. This smoothed downgraded map can be seen in Figure 2.1. An acceptance threshold of 0.75 was then placed on the pixels - any pixel with value less than this is sent to 0 and regarded as part of the new mask, and those with values greater than this were sent to 1. This new binary mask was then applied to each of the `NSIDE` = 64 CMB maps, with 72% of the sky left active for analysis. These maps can be seen in Figure 2.2.

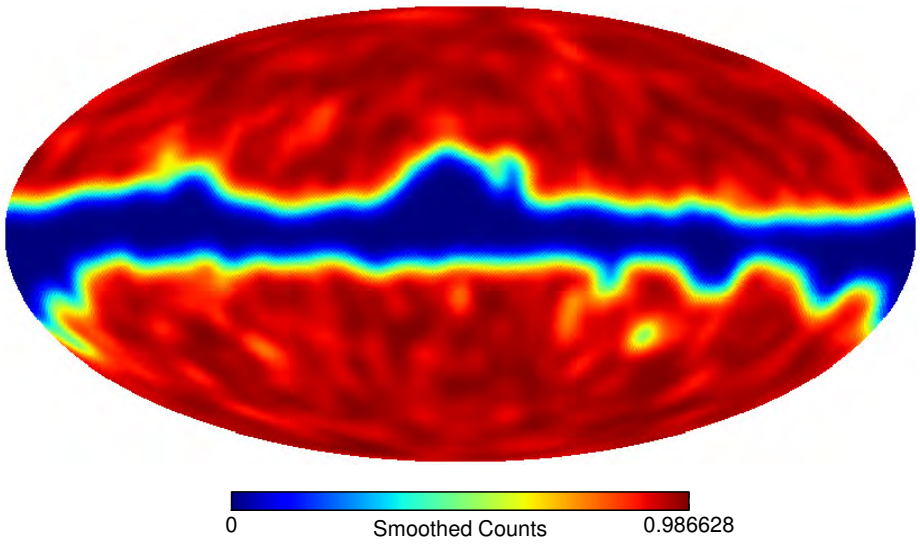

Figure 2.1: The smoothed, downgraded CMB mask. The Planck U73 mask was smoothed using a Gaussian kernel with FWHM = 5.72', and downgraded to a resolution of `NSIDE` = 64. All pixels with a value less than 0.75 are regarded as part of the new mask.

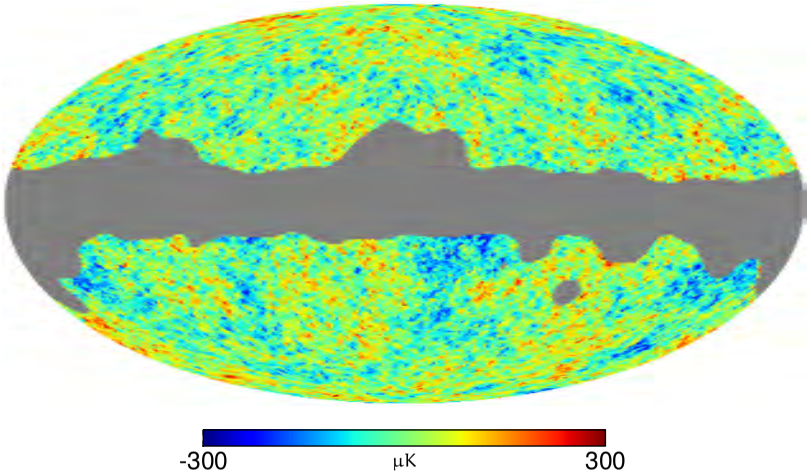

(a) C-R

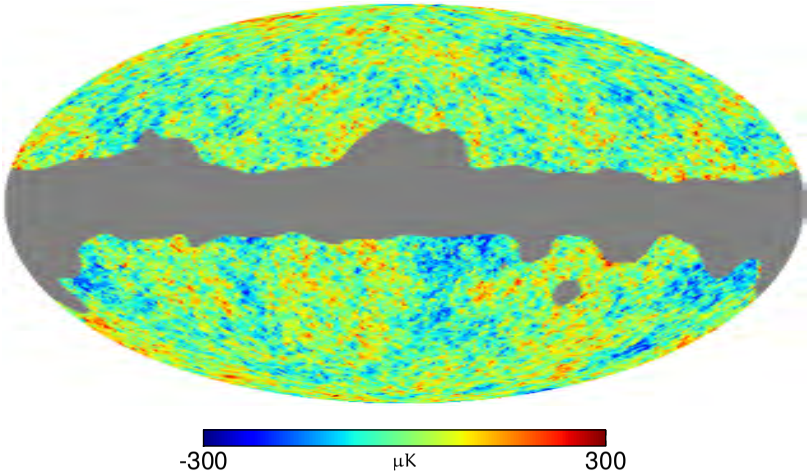

(b) NILC

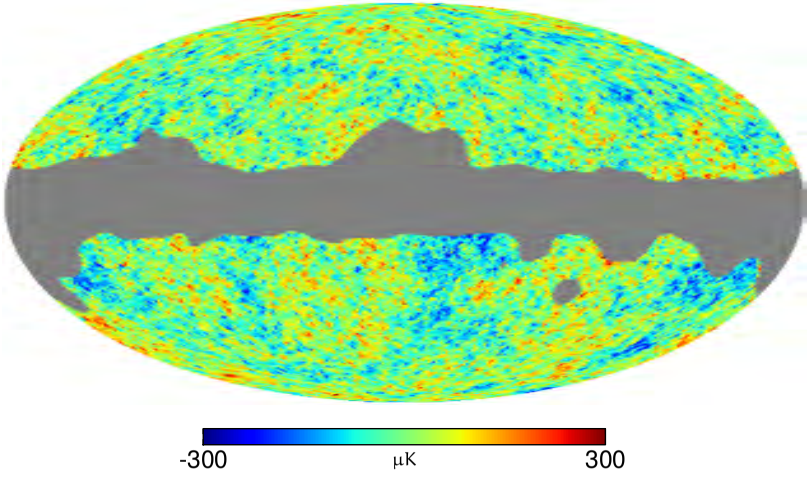

(c) SEVEM

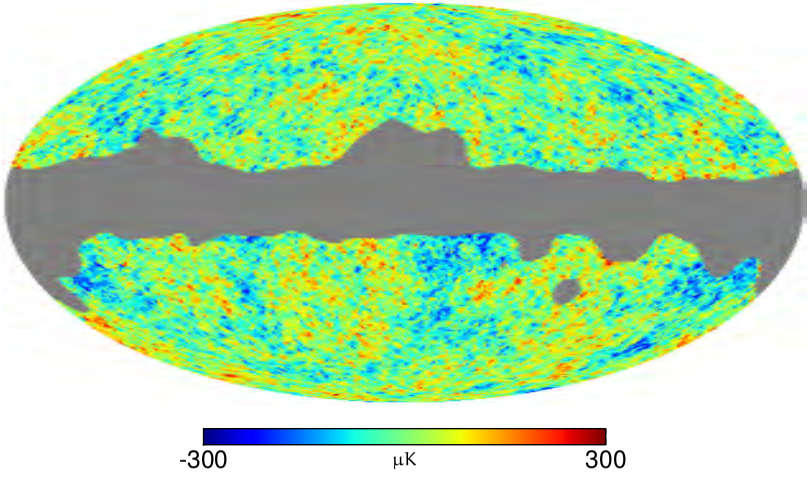

(d) SMICA

Figure 2.2: Mollweide projections in Galactic coordinates of the masked maps of the CMB for each of the four Planck component separation methods. The colour scale indicates the temperature deviation from the mean in μK.

2.4 Photometric Redshift Data

The 3-dimensional galaxy distribution data come from the 2MASS Photometric Redshift catalogue* (2MPZ, Bilicki et al. (2014)). The artificial neural network approach (the ANNz algorithm, Collister & Lahav (2004)) was used to determine the photometric redshifts, trained on spectroscopic redshifts from 2MRS (Huchra et al. 2012), SDSS (Eisenstein et al. 2011), 6dFGS (Jones et al. 2004), 2dFGRS (Colless et al. 2001) and the ZCAT survey compilation (Huchra et al. 1996).

For the entire 2MASS external source catalogue (XSC), there are over 480 000 spectroscopic redshift values available at the time of writing. In the creation of 2MPZ, which is flux-limited in the K_S-band at $K < 13.9$, 310 445 of these, with a median $z = 0.07$, were used as part of the training set to determine photometric redshift values through machine learning for almost 935 000 galaxies from the cross-matched 2MASS XSC (Jarrett et al. 2000), WISE (Wright et al. 2010) and SuperCOSMOS (Hambly et al. 2001) all-sky samples.

2MASS is the most complete, all-sky galaxy catalogue, and the 2MPZ is the only all-sky photometric redshift catalogue, available at the moment. The photometric redshift values achieved in 2MPZ are an improvement in accuracy and number over previous attempts at all-sky 3D catalogues based on 2MASS (Jarrett 2004), with an rms error of around 0.015 (see Bilicki et al. (2014) for more details).

Of the over 934 000 galaxies with photometric redshift values in the 2MPZ, over 932 000 lie between $0.0 < z < 0.3$, the redshift range of interest for this analysis. Figure 2.3 shows a Mollweide projection of the catalogue, with the galaxies colour-coded by redshift. It can be seen that this catalogue is not technically all-sky, as, with any galaxy survey, there is a Zone of Avoidance, as well as regions of incompleteness.

Following the method of Francis & Peacock (2010), three galaxy subsamples were created in photometric redshift shells of thickness $\Delta z = 0.1$, out to z = 0.3. The division of the data set into redshift bins allows for a tomographic approach to the analysis, which should boost the signal of the cross-correlation. This redshift binning does lead to a higher level of shot noise in the data, but this is outweighed by the gains afforded by using three separate data sets. The fact that the theoretical ISW signal is expected to increase with redshift (Francis & Peacock 2010) is additional motivation for this binning. Tomographic analysis with a data set such as WISE would not be possible due to the lack of avaiable redshift information.

The true redshift distribution of the galaxies in each of the shells was found using the spectroscopic redshifts for the relevant subsamples that had them measured (mostly from SDSS), and parametrised as

*http://surveys.roe.ac.uk/ssa/TWOMPZ

$$\frac{\mathrm{d}N}{\mathrm{d}z} \propto \left(\frac{z}{z_*}\right)^a \exp\left\{\left(-\frac{z}{z_*}\right)^b\right\} \tag{2.1}$$

and least squares fitting was done to obtain the various distribution parameters. The distribution parameters are summarised in Table 2.1, and the distributions themselves can be seen in Figure 2.4. Knowledge of this distribution is necessary for the computation of the theoretical auto- and cross-correlation functions. The absolute normalisation of Equation 2.1 is not important in this analysis, as the factors of the normalisation factor cancel out (see Equation 1.5). The number of galaxies in each shell is, however, important in the calculation of the bias value in each shell (see Section 3.1).

Although there are very few galaxies in the shell $0.2 < z < 0.3$, these data are still useful by virtue of the larger volume they represent. This shell is expected to double the total ISW signal, compared to using data just from $z < 0.2$ (Francis & Peacock 2010). However, this last redshift shell needs to be carefully considered - the Malmquist bias is a concern here, as only the most luminous galaxies will have been observed in this region, and they in turn live in clusters. Magnitude cuts need to be made to ensure that this bias is accounted for (see Section 2.5).

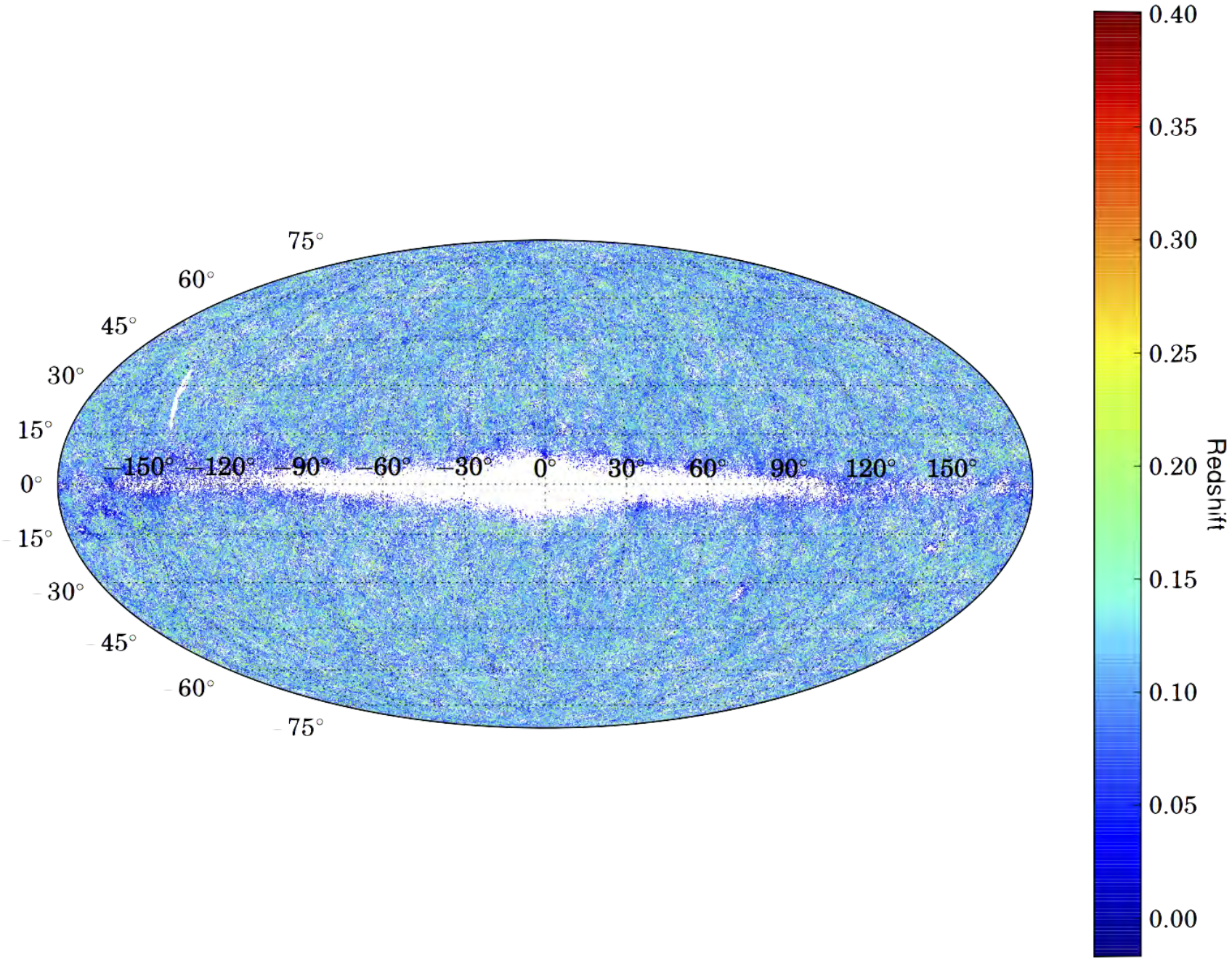

Figure 2.3: Mollweide projection in Galactic coordinates of the the 2MPZ catalogue. The galaxies are colour-coded by redshift.

Table 2.1: The best-fit parameters for the redshift distribution described by Equation 2.1 for each redshift shell. The number of galaxies in each shell, the number having spectroscopic redshift values, as well as the best for values of a, b and z_* are shown.

Photometric redshift	N_{gals}	N_{spec}	a	b	z_*
$0.0 < z < 0.1$	632 512	233 983	0.8689	3.399	0.08418
$0.1 < z < 0.2$	278 454	71 343	7.222	2.372	0.07924
$0.2 < z < 0.3$	21 817	5 119	18.68	3.351	0.1331

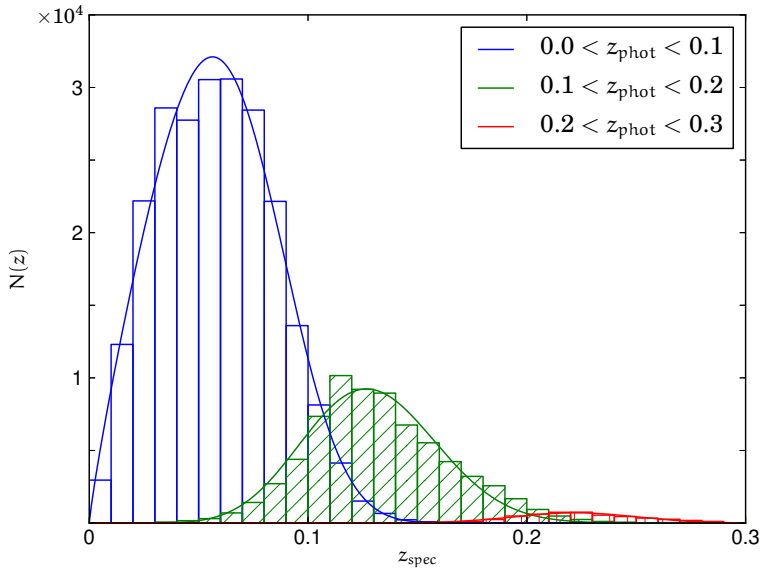

Figure 2.4: Redshift distribution of the galaxies in the range of interest. The histograms show the underlying spectroscopic redshift distribution of the galaxies in each of the photometric redshift-selected shells. The curves are the best fit parametrised redshift distributions, normalised to match these data.

2.5 Dust Maps and Completeness

Following the method of Afshordi et al. (2004), the dust map of Schlegel et al. (1998) was used to determine the regions of the sky where the 2MASS data (and therefore the 2MPZ data) are unreliable.

The 2MASS XSC is unreliable at low Galactic latitudes ($|b| \lesssim 10°$, as well as the bulge), due to confusion in these regions of high stellar density (Jarrett 2004), as well as dust obscuration. A simple cut in latitude would, however, result in a large area of the sky being disregarded, that could otherwise be used in this analysis. Only areas of the sky contaminated by confusion should be excluded.

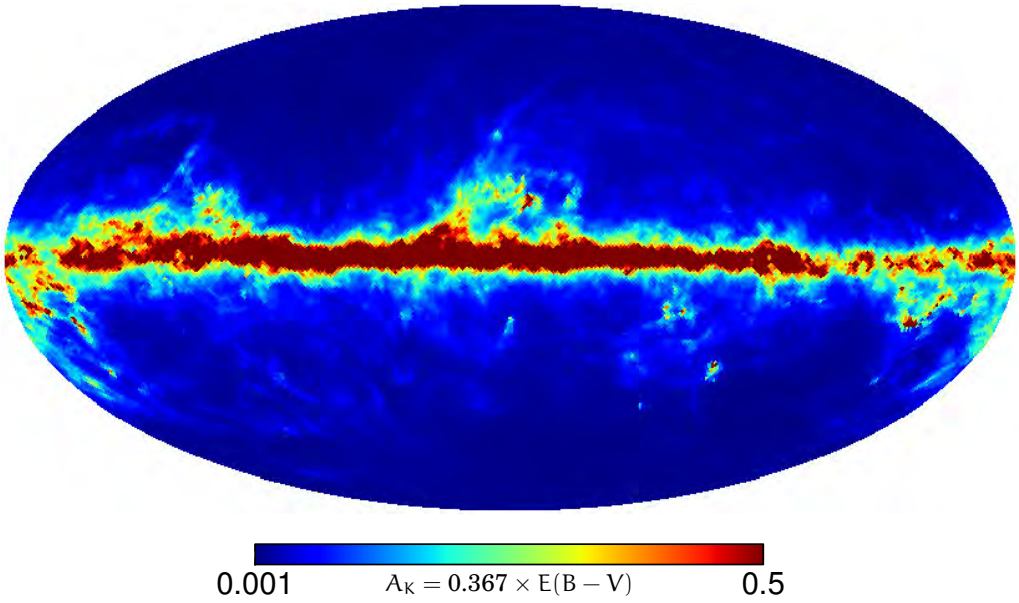

Figure 2.5: Mollweide projection in Galactic coordinates of the optical extinction map of Schlegel et al (1998), converted to K_S-band using the relative extinction coefficient from their Table 6. The map was pixelised with a resolution of NSIDE = 64.

The method used here for the determination of areas of the sky to mask is to use the dust map of Schlegel et al (1998). The original maps* are of the HEALPix resolution of `NSIDE` = 512 - the `healpy` function `ud_grade` was used to downgrade the $E(B-V)$ map to `NSIDE` = 64. The values of $E(B-V)$ were converted to A_K using the K_S-band extinction coefficient $A_K/E(B-V) = 0.367$ taken from Cardelli et al. (1989). The resulting A_K map can be seen in Figure 2.5.

The 2MPZ sample used here was flux limited at $12 < K_S < 13.9$, having been extinction corrected. The bright magnitude limit of $K_S > 12$ was chosen due to the fact that the photometric redshifts are not well constrained here due to problematic WISE and SuperCOSMOS photometry. SuperCOSMOS was compiled using photographic plates, whose photometric quality is not high, and for WISE, point source photometry was used for all sources, so photometry of bright galaxies of large angular size will not be accurate. The faint magnitude limit of $K_S < 13.9$ is roughly the completeness limit of 2MASS (Jarrett 2004). The validity of this completeness limit for 2MPZ was independently verified.

As per Afshordi et al. (2004), the galaxies were split into 4 magnitude bins. The average number of galaxies per pixel was then calculated as a function of K_S-band extinction for each of the magnitude bins, as per Figure 2 of Afshordi et al. (2004). The 49 152 pixels over

*http://www.astro.princeton.edu/∼schlegel/dust/

the sky were binned according to their values in the extinction map - these same pixels were then identified in each of the magnitude-limited galaxy density maps, and the mean density over these pixels was calculated. The results of this analysis can be seen in Figure 2.6.

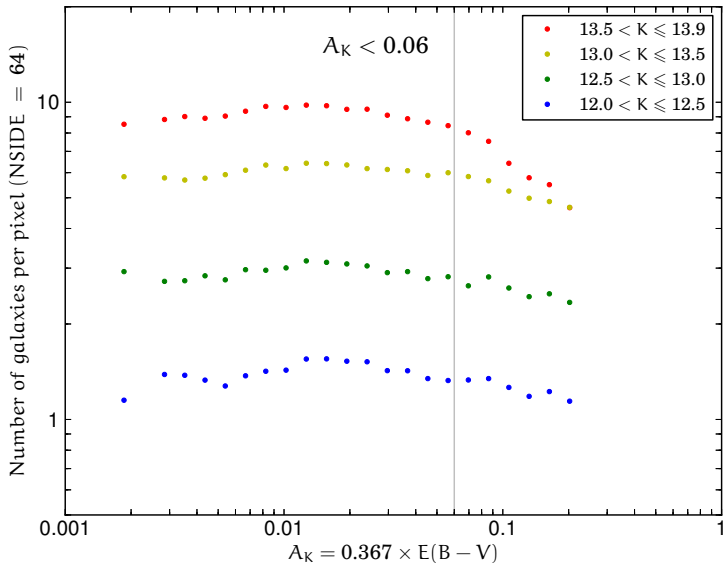

Figure 2.6: The average number of galaxies per pixel, as a function of extinction. The fainter galaxies (K $>$ 13.0) show a drop-off around $A_K \sim 0.07$. Regions of the sky with $A_K > 0.06$ were subsequently masked off.

It can be seen that for the faintest magnitude bins ($K_S > 13.0$) the mean density values drop off around $A_K \sim 0.07$. The value $A_K \geqslant 0.06$ was therefore conservatively chosen to define the pixels that would be masked out. This limit for the mask leaves 71% of the sky unmasked.

2.6 Creation of Galaxy Overdensity Maps

The entire 2MPZ catalogue was first divided by redshift into three shells, with $0.0 < z < 0.1$, $0.1 < z < 0.2$ and $0.2 < z < 0.3$ respectively. The given values of galactic latitude and longitude were then converted to `HEALPix` pixel values, to create density maps for each shell with a resolution of `NSIDE` = 64.

Following the method of Francis & Peacock (2010), each of these density maps was then smoothed using a Gaussian kernel, with FWHM = $100'$ for $0.0 < z < 0.1$ and $0.1 < z < 0.2$, and FWHM = $200'$ for $0.2 < z < 0.3$. A larger smoothing kernel was used in the last shell to compensate for the lower average number density of pixels in this shell. The resulting maps were then masked, with the masked pixels dictated by the A_K values as described in Section 2.4, leaving an active area of 71% of the sky.

The overdensity value for each pixel was then calculated, resulting in the masked overdensity maps seen in Figure 2.7.

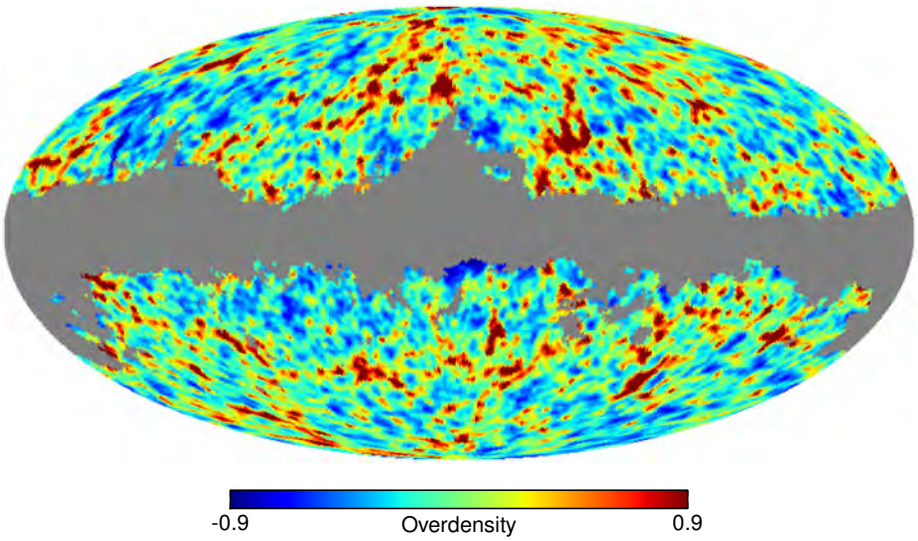

(a) $0.0 < z < 0.1$

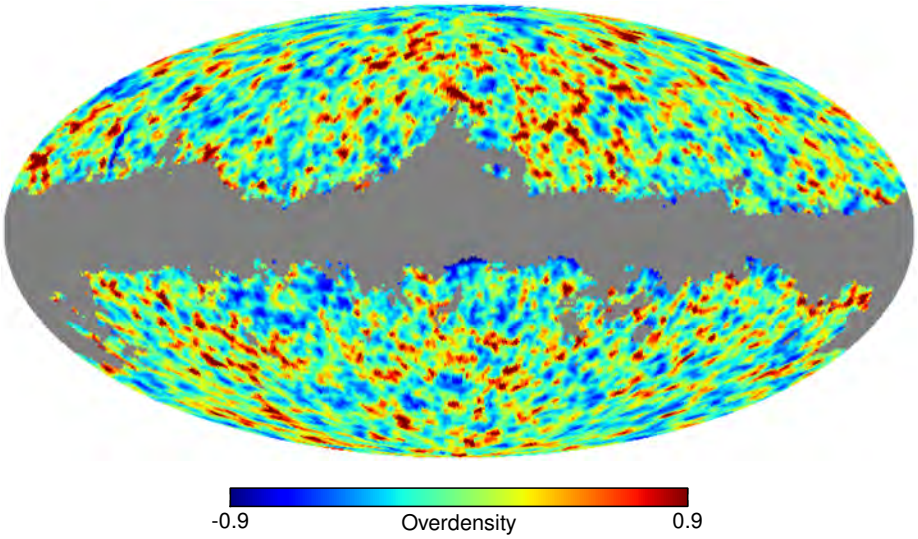

(b) $0.1 < z < 0.2$

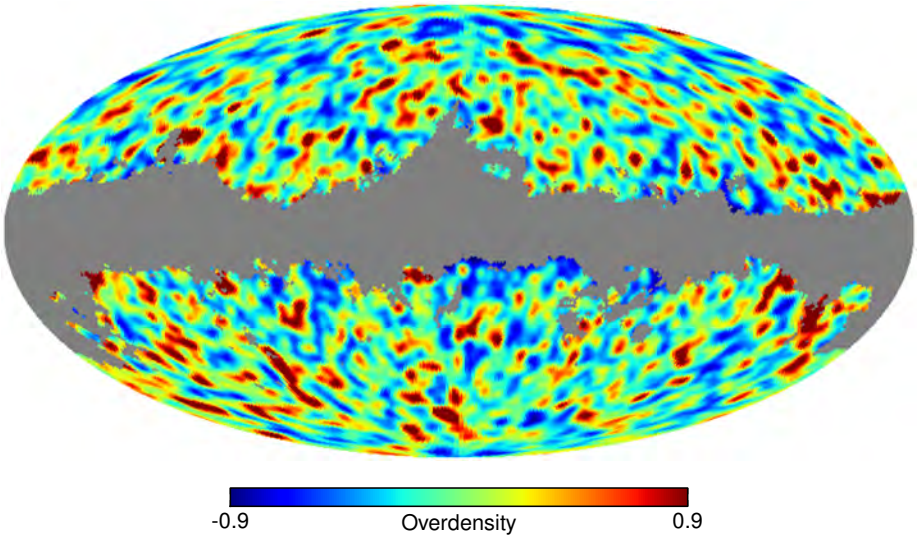

(c) $0.2 < z < 0.3$

Figure 2.7: Mollweide projections in Galactic coordinates of the masked maps of the 2MPZ galaxy overdensity in each of the 3 redshift shells: $0.0 < z < 0.1$ (top), $0.1 < z < 0.2$ (middle) and $0.2 < z < 0.3$ (bottom). The maps are colour-coded by the overdensity value in each pixel. The original density maps were first smoothed with a Gaussian kernel of FWHM $= 100'$ for the first and second shells, and FWHM $= 200'$ for the third shell.

Chapter 3

Cross-Correlation Results

This chapter presents the key results of the thesis, namely the cross-correlation of the Planck and 2MPZ data. First, however, the effective galaxy bias values for each shell need to be estimated. This is done via galaxy auto-correlation analysis. Such estimates are limited by the shot noise, which will be discussed first.

3.1 Shot Noise Removal

Due to discrete sampling of the density field by observed galaxies, their auto-correlation measurements will be limited by shot noise on small angular scales.

The shot noise in each shell was calculated using randomised galaxy overdensity maps, and compared to the theoretical prediction for high ℓ.

The number of galaxies in each redshift shell N_{gal} was used to create a list of random Galactic latitude and longitude values. This list was pixelised to form a random galaxy density map, which was then converted to an overdensity map. The galaxy auto-correlation power spectrum C_{gg} was then calculated for the overdensity map to $\ell = 110$. This is the default value of ℓ for which `healpy` calculates correlation functions, and is more than high enough for this purpose.

The value of C_{gg} for these maps in each shell is predicted, at high ℓ, to be

$$C_{\mathrm{gg}} = \frac{4\pi\ f_{\mathrm{sky}}}{N_{\mathrm{gal}}} \tag{3.1}$$

where f_{sky} is the fraction of the overdensity map that has not been masked. This prediction for shot noise is derived from the fact that we assume the galaxy observations to represent Poisson sampling of a continuous underlying galaxy density field.

This prediction was shown to be true for all three redshift shells, and the constant value of $C_{\rm gg}$ for each shell was subtracted from each of the galaxy auto-correlation functions presented hereunder.

3.2 Auto-Correlation and Bias Fitting

Recall equation 1.11, the expression for the predicted galaxy auto-correlation function derived using the Limber approximation:

$$C_{\rm gg}(\ell) = b^2 \int {\rm d}r \, \frac{\Theta^2}{r^2} \, g^2 \, P\left(\frac{\ell + 1/2}{r}\right).$$

Comparing this value for the theoretical prediction with the value measured observationally ($C_{\rm gg}^{\rm obs}$) for a given power spectrum and redshift distribution is a way of estimating the galaxy bias.

These theoretical predictions for the galaxy auto-correlation function in each redshift shell were computed, with the integrals having been performed using `Mathematica`*. An initial bias value of 1 was used in the calculations, to allow for least squares fitting of the bias value for the theoretical and observed functions. The power spectrum $P(k)$ was obtained using `CAMB`, with the Planck best-fit cosmological parameters shown in Table 1.1.

The best-fit bias value was then determined through least squares fitting of the theoretical $C_{\rm gg}$ to the observed values in each redshift shell.

The $C_{\rm gg}$ values for the data were computed to an $\ell = 110$, using the `healpy` function `anafast`. Each of these $C_{\rm gg}$ values was then rescaled by a factor of $f_{\rm sky}^{\rm g}$, the fraction of the galaxy overdensity maps left unmasked, as in Section 3.1, after which the constant shot noise for each shell was subtracted. The resulting values were then truncated in ℓ at the first point where $C_{\rm gg}^{\rm SN} > C_{\rm gg}^{obs}$, so that only positive values of $C_{\rm gg}^{\rm obs} - C_{\rm gg}^{\rm SN}$ remained.

The uncertainty in the measurement of the observed $C_{\rm gg}$ values was calculated as (Rassat et al. 2007)

$$\sigma^{\rm obs} = \sqrt{\frac{2}{f_{\rm sky}^{\rm g}(2\ell+1)}} \, C_{\rm gg}^{\rm obs} \tag{3.2}$$

The theoretical and observed $C_{\rm gg}$ values, as well as the uncertainties, were then binned, in 5 logarithmically spaced bins in ℓ, with a maximum ℓ of 62 for the first and second redshift shells, and a maximum ℓ of 35 for the third. The difference comes about due to the shot noise levels in each shell - the third shell was truncated at $\ell = 35$ after shot noise removal to ensure

*Theoretical predictions kindly provided by Dr. M. Bilicki.

Table 3.1: The bias values for each redshift shell, acquired through least squares fitting. The theoretical prediction for the galaxy auto-correlation function was fitted to the shot noise-subtracted auto-correlation function from the data.

Redshift	Bias	Minimum χ^2	σ_b
$0.0 < z < 0.1$	1.07	1.44	0.07
$0.1 < z < 0.2$	1.29	2.67	0.08
$0.2 < z < 0.3$	2.08	3.46	0.20

that only positive values of C_{gg} were used and the shot noise-dominated scales were excluded.

The bias value was then varied, and the χ^2 parameter was calculated as

$$\chi^2 = \sum_m \frac{\left(b^2\, C_m^{\mathrm{theor}} - C_m^{\mathrm{obs}}\right)^2}{\sigma_m^2} \tag{3.3}$$

where m is the bin index. Minimisation of the χ^2 parameter provided the best-fit value of the bias for each redshift shell.

Table 3.1 shows the best-fit bias value for each shell, and Figure 3.1 shows the binned $C_{\mathrm{gg}}^{\mathrm{obs}}$ values with the binned values of $b^2 C_{\mathrm{gg}}^{\mathrm{theor}}$.

Whilst it is possible that the calculation of the bias values has been influenced by systematic effects in the galaxy data, steps have been taken to mitigate this. The homogeneity of the galaxy data was tested, and magnitude cuts were made before the overdensity maps were created (see Section 2.5). No known calibration issues are present in the 2MPZ, and, whilst no galaxy catalogue is perfect, all uncertainties associated with the galaxy data have been determined using sophisticated mock galaxy maps (see Section 3.3). As such, reasonable confidence can be held in these values.

When compared to the best-fit bias values computed by Francis & Peacock (2010) using photometric redshift data in each shell, these values are consistently lower, with the difference increasing with redshift. As the bias fitting assumes a fixed cosmological model and fixed parameters, the uncertainties shown in Table 3.1 quantify only the best fit of the bias, resulting in the two sets of bias values not being directly comparable. The differences could be due to the different sets of cosmological parameters used in the computation of the theoretical predictions of the galaxy auto-correlation functions, as Francis & Peacock (2010) were using the WMAP parameters. They could also be attributed to the fact that the photometric redshifts used by Francis & Peacock (2010) are less accurate than those in 2MPZ, and that they chose a K_S-band limit of 13.8 as opposed to the value of 13.9 used here.

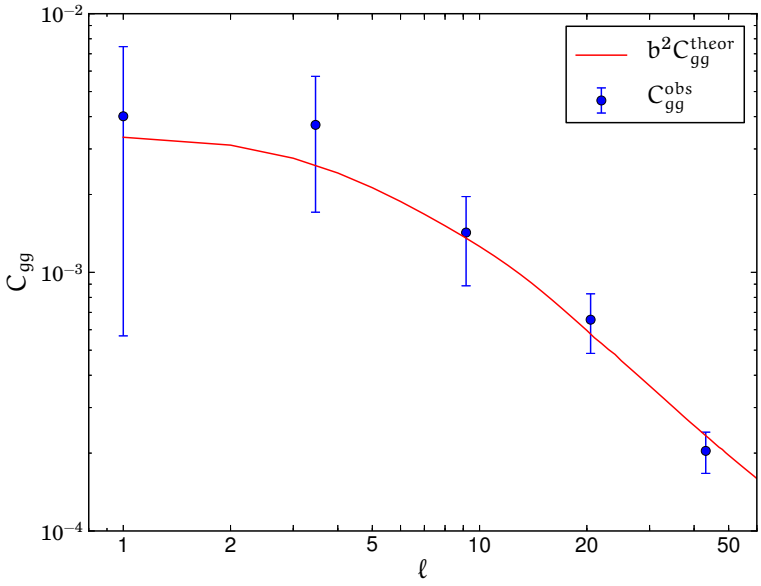

(a) $0.0 < z < 0.1$

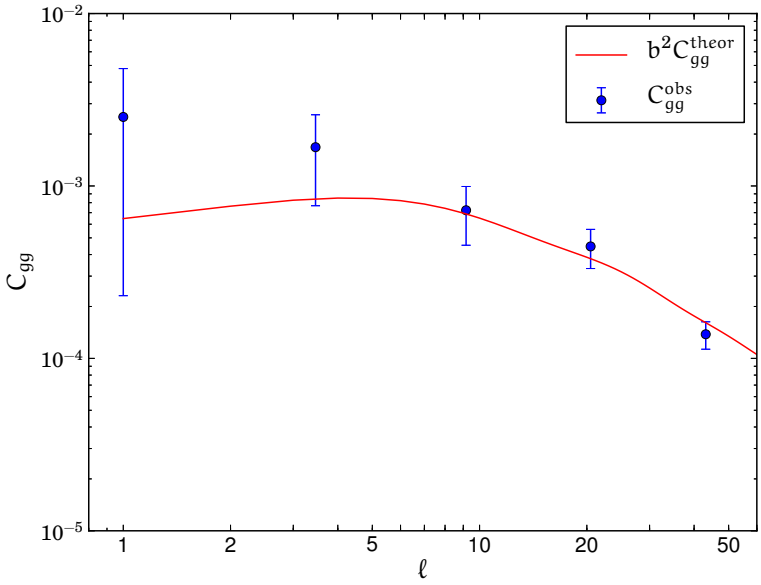

(b) $0.1 < z < 0.2$

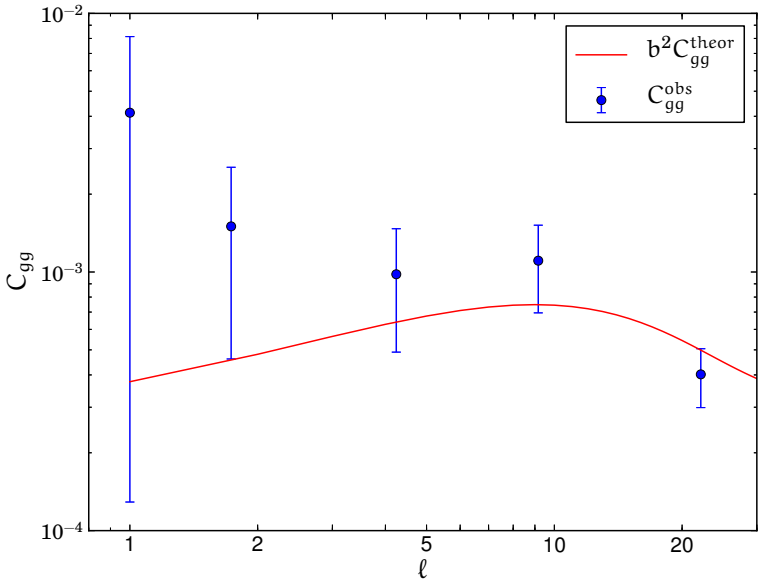

(c) $0.2 < z < 0.3$

Figure 3.1: Plots of the galaxy auto-correlation functions for each of the three redshift shells, with the bias-rescaled theoretical predictions for each shell. The uncertainties were calculated using the theoretical prediction values in each bin.

3.3 Cross-Correlation

Spherical harmonics for all of the galaxy overdensity and CMB anisotropy maps were computed using `healpy`. The cross-correlation function can be expressed as

$$C_{\mathrm{gT}} = \frac{1}{(2\ell+1)} \sum_{m=-\ell}^{\ell} \frac{a^{\mathrm{g}}_{\ell m}}{\sqrt{f^{\mathrm{g}}_{\mathrm{sky}}}} \frac{a^{\mathrm{T}*}_{\ell m}}{\sqrt{f^{\mathrm{T}}_{\mathrm{sky}}}} \tag{3.4}$$

where the $a_{\ell m}$ are the spherical harmonic coefficients and the f_{sky} are the fractions of the sky left unmasked in the galaxy and CMB maps respectively. The `healpy` function `anafast` was used to calculate the C_{gT} values, which were subsequently normalised by each of the required factors of $\sqrt{f_{\mathrm{sky}}}$. `anafast` calculates the spherical harmonic coefficients by assigning masked pixels a temporary value of zero. In this way, the mask is taken into account, with the factor of f_{sky} used to compensate for the loss of power the masked pixels bring about. The resulting values were then binned following the method of Francis & Peacock (2010), in 5 logarithmically spaced bins with $3 \leq \ell \leq 30$. Following Rassat et al. (2007), $\ell = 2$ is excluded due to its anomalously low power in the CMB.

This cross-correlation was performed for all 4 CMB maps and all 3 redshift shells. The resulting values of C_{gT} were found to be consistent over all 4 CMB maps within each redshift shell.

Recall Equation 1.9, the theoretical prediction for the cross-correlation function, derived using the Limber approximation:

$$C_{\mathrm{gT}}(\ell) = \frac{-b\, H_0^2\, \Omega_m\, T}{c^3(\ell+1/2)^2} \int \mathrm{d}r\; \Theta(r)\; H\; g^2(f-1)\; P\left(\frac{\ell+1/2}{r}\right)$$

These theoretical predictions were computed for each redshift shell, with the integrals having been performed using `Mathematica`*. A bias value of 1 was again used in the calculations. Before further analysis and plotting, these predictions were then multiplied by the best-fit bias value for each shell found in Section 3.2.

The uncertainties associated with the measurements were obtained using simulated galaxy overdensity and CMB anisotropy maps. The `healpy` function `synfast` was used to create all-sky maps from the CMB power spectrum, whilst the galaxy maps were simulated using a lognormal realisation of the matter overdensity field (Coles & Jones 1991).

`CAMB` was used to produce the CMB power spectrum. The cosmological parameters used were the Planck best-fit parameters, listed in Table 1.1. The resulting power spectrum was then truncated to the range in ℓ of interest, and input to `synfast`, resulting in 100 simulations of the CMB with the resolution parameter of `NSIDE` = 64 as the data.

*Theoretical predictions kindly provided by Dr. M. Bilicki.

Mock galaxy distribution maps were kindly provided by Dr. David Alonso at the University of Oxford. 100 lognormal mock galaxy catalogs were created, using the following method:

- A Gaussian realisation of the matter overdensity field in Fourier space was generated, using the linear power spectrum for the specified cosmology
- This was then transformed to real space, and the linear clustering bias was added
- The continuity equation was used to infer the corresponding velocity field
- A lognormal transformation was applied to the overdensity field
- The resulting density field was Poisson sampled, taking into account the redshift distribution of the underlying catalog, to get galaxy positions and redshifts
- The redshift distortion was calculated from the velocity field, and was added to the cosmological redshifts
- The resulting redshifts were then perturbed with the photometric redshift distribution of the catalog

A full description of the method can be found in the Appendix of Alonso et al. (2014). These maps were then pixelised and converted into overdensity maps with `NSIDE` = 64, as per the 2MPZ maps.

Cross-correlation of 100 mock CMB maps and 100 mock galaxy maps was performed, resulting in 10 000 data points with which to calculate uncertainties. The resulting cross-correlation functions were binned as per the data, and the mean and standard deviation of the binned values were computed. The mean of the cross-correlations from the simulated maps was found to be consistent with zero, as expected. The standard deviation values were used as the error bars for the observed C_{gT} values, centered on the data points.

Figure 3.2 is a key plot showing the results of the cross-correlation analysis. The result for only the SMICA CMB map is shown in each panel for clarity, but very similar results were seen for all 4 CMB maps.

The ISW signal is expected to be the strongest in the third redshift shell ($0.2 < z < 0.3$), as the strength of the ISW effect is expected to increase with increasing redshift (Francis & Peacock 2010).

The significance of these results will be quantified in the following chapter.

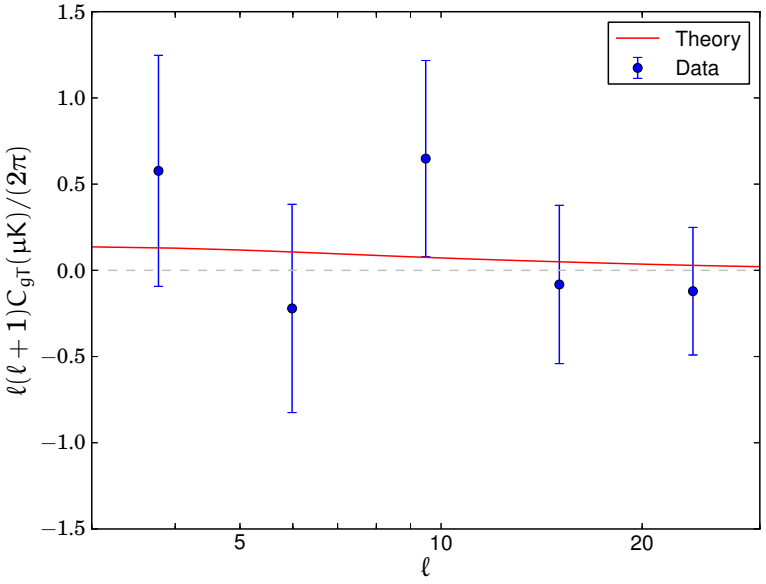

(a) $0.0 < z < 0.1$

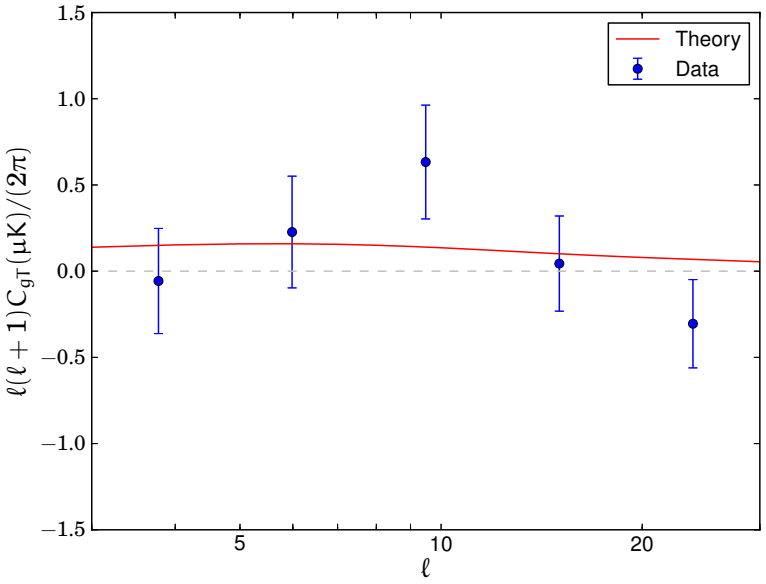

(b) $0.1 < z < 0.2$

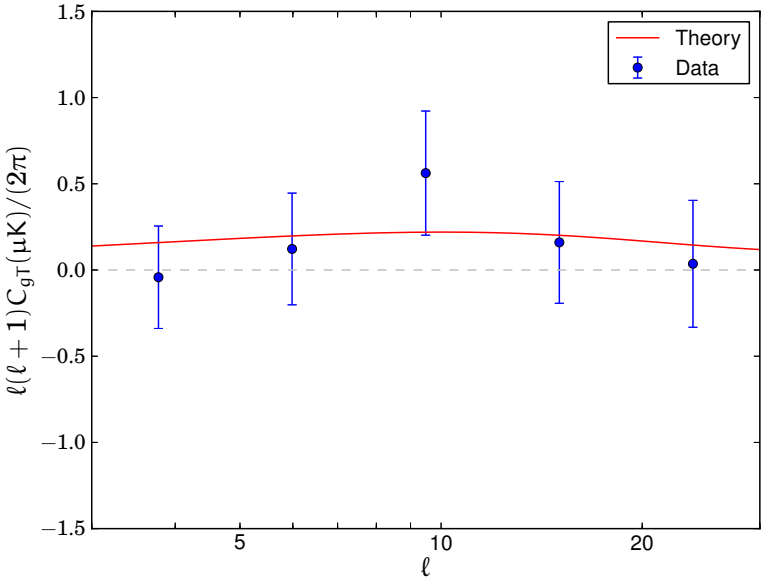

(c) $0.2 < z < 0.3$

Figure 3.2: Plots of the cross-correlation functions for each of the three redshift shells. The points displayed are the values calculated using only the SMICA CMB map for clarity.

Chapter 4

Significance of the Detection

4.1 Covariance and Hypothesis Testing

To help access the significance of an ISW effect detection, two hypotheses are tested: a null hypothesis of no cross-correlation, and an alternative hypothesis represented by the theoretical predictions, i.e. the cross-correlation expected in a ΛCDM universe (see Section 1.2).

By this stage we have the cross-correlation from the data, theoretical predictions given our adopted cosmology and empirical galaxy catalog, and error bars estimated from simulated galaxy and CMB data. These data, combined with a null hypothesis of $C_{\mathrm{gT}}(\ell) = 0$ for all multipoles, are sufficient for hypothesis testing.

A full covariance matrix approach was taken in the determination of the χ^2 statistic, which was used to determine which of the hypotheses is preferred. When using χ^2 to evaluate goodness of fit, we are basically fitting a line to the observed points. As the observed points in this case are at a number of different values of ℓ, we need to check that these points are uncorrelated before proceeding with the hypothesis testing.

The covariance matrix for each redshift shell was computed using simulated data (see Section 3.3).

The covariance matrix is calculated as

$$\mathbf{C}_{ij} = \langle (s_i - \langle s_i \rangle)(s_j - \langle s_j \rangle) \rangle \tag{4.1}$$

where the s_i are the binned values of the cross-correlation function from each of the simulated data runs, and the $\langle s_i \rangle$ are the mean values of the cross-correlation function over all simulated data runs. These mean values were found to be consistent with zero, but the calculated values were used for the sake of consistency.

The χ^2 statistic for each shell was then calculated as

$$\chi^2 = \sum_{i,j} d_i \left(\mathbf{C}^{-1}\right)_{ij} d_j \tag{4.2}$$

where $\mathbf{C}_{ij}$ is the covariance matrix from the simulated data. The d_i here are the values of

$$d_i = C^{\mathrm{data}}_{\mathrm{gT},i} - C^{\mathrm{hyp}}_{\mathrm{gT},i} \tag{4.3}$$

where the $C^{\mathrm{data}}_{\mathrm{gT},i}$ are the measured cross-correlation values in each bin. For the null hypothesis, the values of $C^{\mathrm{hyp}}_{\mathrm{gT},i}$ are zero in every bin, and for the alternative hypothesis, the values of $C^{\mathrm{hyp}}_{\mathrm{gT},i}$ are given by the theoretical predictions multiplied by the best-fit bias value in each shell.

Plots of the covariance matrix for each bin are shown in Figure 4.1. It can be seen that the non-diagonal elements of each of the matrices are very close to zero – this is encouraging, as it indicates that there is very little cross-talk between the bins, and consequently means that the use of the χ^2 statistic is justified and meaningful. However, for the sake of self-consistency, the full covariance matrix is used in the calculation of χ^2.

The likelihood of each hypothesis can then be expressed as

$$\mathcal{L} \propto |\mathbf{C}^{-1/2}| \exp\{-\left(\mathbf{d}^{\mathrm{T}}\mathbf{C}^{-1}\mathbf{d}\right)/2\} \tag{4.4}$$

where $\mathbf{C}$ is the covariance matrix and $\mathbf{d}$ is the data vector whose components are described in Equation 4.3.

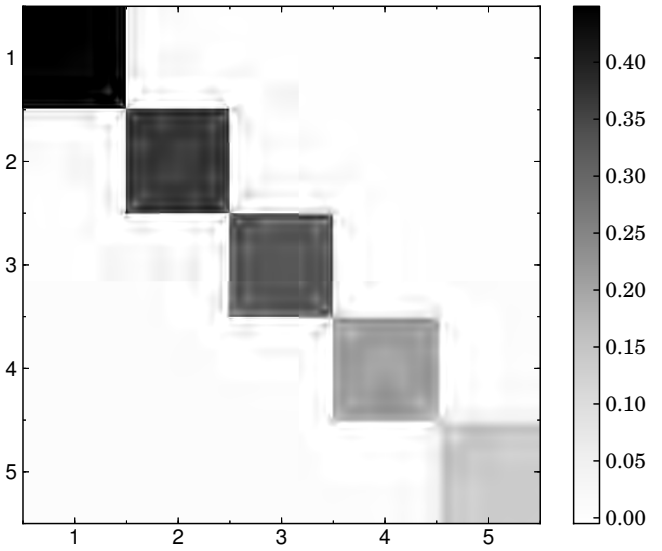

(a) $0.0 < z < 0.1$

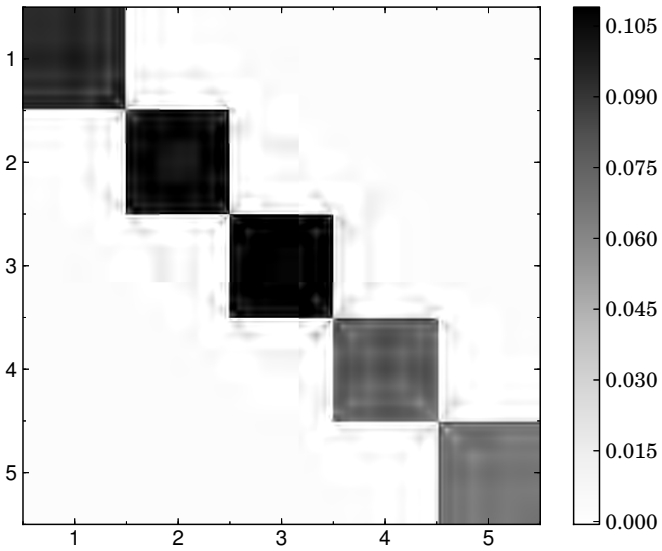

(b) $0.1 < z < 0.2$

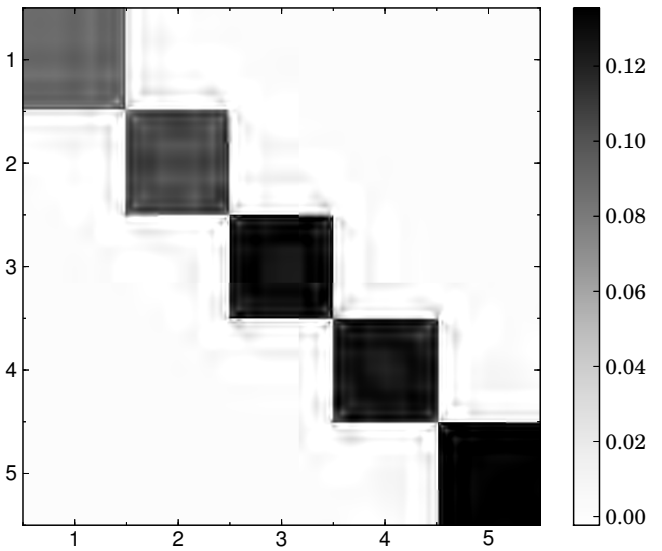

(c) $0.2 < z < 0.3$

Figure 4.1: The full covariance matrices for each of the three redshift shells. Rows and columns are indexed by bin number. It can be seen that there is very little cross-talk between the bins, as the off-diagonal elements are very close to zero. It should be noted that the scales differ for each plot.

4.2 Likelihood of Alternative Hypothesis

The ratio of the likelihood values of each of the hypotheses is the key indicator of whether or not a statistically significant detection of the ISW effect has been made. This ratio of likelihoods can be expressed in terms of the difference of the χ^2 values over all 3 redshift shells

$$-2\ln\{\frac{\mathcal{L}_0}{\mathcal{L}_1}\} = \Delta\chi^2 \tag{4.5}$$

where $\Delta\chi^2$ is the sum of the difference between the values of χ^2 for the null and alternative hypotheses in each of the redshift shells. This expression can then be rearranged to give the total likelihood ratio:

$$\frac{\mathcal{L}_1}{\mathcal{L}_0} = \exp\left(\Delta\chi^2/2\right) \tag{4.6}$$

When expressed like this, it can be see that a likelihood ratio > 1 therefore shows a preference for the alternative hypothesis.

A likelihood ratio approach is taken in the determination of the statistical signficance of the detection primarily so that this result can be compared to that of Francis & Peacock (2010). Their method is followed in order to examine whether improved photometric redshifts will give improved odds of a detection. A full maximum likelihood approach could also be used to to evaluate the significance of the detection, but would involve steps such as the varying of the cosmological model parameters and would be beyond the scope of this work.

A summary of the χ^2 values for each of the redshift shells and for each of the methods of CMB component separation can be seen in Table 4.1. The mean $\Delta\chi^2$ values over all four CMB maps for each redshift shell, shown in the last row, are all positive, indicating a preference for the alternative hypothesis in every shell.

The total value of $\Delta\chi^2$ is 2.43, which leads to a total likelihood ratio of 3.37:1. As the total likelihood ratio is greater than one, this indicates an overall preference for the alternative hypothesis.

As a covarince matrix approach has been taken in the calculation of the statistical significance of the detection, it is difficult to incorporate errors such as those found on the best-fit bias values. The statistical significance of the result would decrease slightly had these additional errors been included in the analysis.

Auto-correlation between the various galaxy maps was also explored as a possible influence on the statistical significance of the result. In each case, the auto-correlation between

Table 4.1: A summary of the χ^2 values calculated for each redshift shell and for each CMB component separation method. The subscript H_0 denotes the null hypothesis of zero cross-correlation, whilst the subscript H_1 denotes the alternative hypothesis described by the theoretical prediction in each redshift shell. The alternative hypothesis is preferred in each of the redshift shells, most strongly in the third shell.

	$0.0 < z < 0.1$		$0.1 < z < 0.2$		$0.2 < z < 0.3$	
CMB Map	$\chi^2_{H_0}$	$\chi^2_{H_1}$	$\chi^2_{H_0}$	$\chi^2_{H_1}$	$\chi^2_{H_0}$	$\chi^2_{H_1}$
C-R	2.34	2.07	6.19	5.59	2.65	1.39
NILC	2.37	2.05	5.91	5.14	2.88	1.30
SEVEM	2.41	2.12	5.87	5.13	2.79	1.21
SMICA	2.36	2.05	5.87	5.13	2.83	1.56
Mean	2.37	2.07	5.96	5.25	2.79	1.37
$\Delta\chi^2$	0.30		0.71		1.42	

each pair of galaxy maps was found to be negligibly low – around 1% of the cross-correlation signal. This can therefore be assumed not to influence the significance of the result.

When the values shown in Table 4.1 are compared to those of Francis & Peacock (2010), particularly those of their Table 3 where the bias values calculated from photometric redshifts are used, it can be seen at first glance that a stronger preference for the alternative hypothesis is found in this work. Whilst in their work, the alternative hypothesis was only preferred in the first two redshift shells, here a positive value of $\Delta\chi^2$ is found in all 3 shells, with the largest difference, and therefore the strongest preference, being found in the third redshift shell.

The strength of the preference for the alternative hypothesis can be explored using the Jeffreys scale (Jeffreys 1961). This scale says that the likelihood ratio K with value $1 < K < 3$ is a result that is barely worth mentioning, while $3 < K < 10$ is substantial.

Another scale, introduced by Kass & Raftery (1995), judges the strength of the detection using $D = 2 \ln K$ ($\Delta\chi^2$ here). According to this scale, $0 < D < 2$ is not worth more than a bare mention, whilst $2 < D < 6$ is a positive detection.

The result presented here, whilst falling into the category of a positive detection on both scales, is so close to the edge of no statistical significance that it is worthwhile to explore all possible circumstances regarding detection.

Further discussion of the strength of the detection and the reasons for it follow in Chapter 5.

Chapter 5

Discussion

5.1 Discussion

Whilst the result seen in Chapter 4 shows an improvement over that of Francis & Peacock (2010), the low statistical significance of the detection needs to be carefully considered.

The improvement in the likelihood of detection in this work comes about primarily as a result of the greater accuracy of the photometric redshift values used. Whilst the new Planck CMB maps were used here, as opposed to the use of WMAP data by Francis & Peacock (2010), the main difference in these CMB data is an improvement in angular resolution. The large-angle nature of the ISW effect led to the resolution of the CMB maps being downgraded in both cases, so this does not explain the difference in the results.

The photometric redshift catalogue used in this work has an rms error $z_{\rm phot} - z_{\rm spec}$ less than half that of the data used by Francis & Peacock (2010). The fact that more of the galaxies are being placed in the correct redshift bin results in the galaxy distribution $\mathrm{d}N/\mathrm{d}z_{\rm phot}$ being a better reflection of the true distribution of the galaxies in the local Universe, and therefore more accurate prediction and measurement of the ISW effect.

The low statistical significance of the result can be attributed primarily to 2MASS being used as the source for the photometric redshift catalogue. It was shown by Francis & Peacock (2010) that 2MASS is expected to perform poorly at this kind of ISW testing, as it is simply too shallow in terms of redshift. They showed that imposing a fainter magnitude limit – i.e. adding more galaxies in the range $0.1 < z < 0.3$ to the catalogue with characteristic $z_{\rm max} = 0.3$ – would not make a significant difference in the chances of detection. Provided there are enough galaxies within this range to keep shot noise at a minimum, there is little to gain by adding more galaxies in this range.

They go on to show that one way to improve the chances of a conclusive rejection of the

null hypothesis would be to increase the depth of the photometric redshift catalogue. They simulate a galaxy catalogue with $z_{\rm max} = 0.7$ and characteristic redshift $z_{\rm m} = 0.3$, using the known redshift distribution in each shell of width $\Delta z = 0.1$ for $z < 0.3$, and a Gaussian distribution of width $\sigma = 0.03(1 + z)$ (the rms error in $z_{\rm phot} - z_{\rm spec}$ found for their original catalogue), centred at the midpoint of each subsequent shell, out to $z = 0.7$. The found that the increase in depth would greatly improve the chances of a strong ISW detection.

The best step forward in ISW detection with photometric redshifts would therefore be construction of a catalogue with deeper and more accurate redshift values.

5.2 Comparison to Previous Works

While this work has been based primarily on the method used by Francis & Peacock (2010), it is useful to consider the results achieved by other authors using similar methods and data.

The results obtained through ISW analysis by other teams using 2MASS as the source of the galaxy overdensity data were summarised in Section 1.3. Other than Afshordi et al. (2004), no statistically significant detections were made. This work therefore represents an improvement over most of the previous results, as it falls just over the point of a substantial detection on the Jeffreys scale.

Comparing this work further to that done by Francis & Peacock (2010), it must be noted that this work represents an improvement over their results in every way. The $\Delta\chi^2$ values found here are larger than theirs in every redshift shell, indicating an improvement in the detection of the ISW in every case. The galaxy data used are essentially the same in both this case and theirs - the improvement in the rms error in the photometric redshifts from $\sigma = 0.033$ to $\sigma = 0.015$ is the primary reason for the increased significance of the detection.

Chapter 6

Conclusion

6.1 Conclusion

A measurement of the integrated Sachs-Wolfe effect was here made through correlation of the Planck maps of the CMB temperature anisotropies and galaxy overdensity maps from the 2MASS Photometric Redshift catalogue as a tracer of the large-scale structure. Detection of the ISW effect was found to be preferred over no detection in three redshift shells of width $\Delta z = 0.1$ out to $z = 0.3$, with a total likelihood ratio of $3.4 : 1$ in favour of detection. The result, while not quite a statistically significant detection of the ISW effect, is more than twice improved over that found previously by Francis & Peacock (2010) with similar methodology. The improvement in the detection is due primarily to the accuracy of the photometric redshift values used, as opposed to being due to improvement in the angular resolution of the CMB maps or the number of galaxies over the redshift range $0.0 < z < 0.3$. Improvement in the depth and accuracy of photometric redshift catalogues is the next step forward in terms of detection of the ISW effect using this method.

6.2 Future Work

A new photometric redshift catalogue will provide deeper photometric redshift values, with a far larger volume, for future ISW measurements. This catalogue (Bilicki et al. 2014, in prep) performs a cross-match of two large all-sky catalogues, AllWISE and SuperCOSMOS, and contains 22 million galaxies over 3π sr of the sky. The ANNz framework is used to derive photometric redshifts, trained on GAMA and SDSS DR10 spectroscopic redshifts. This new sample has a median redshift of $z_{med} \sim 0.2$, but has a broad $\mathrm{d}N/\mathrm{d}z$ distribution out to $z \sim 0.5$. Following Francis & Peacock (2010), it is expected that this new catalogue should give a stronger ISW signal than 2MPZ has.

This new catalogue, with its combination of accuracy and greater depth of photometric redshifts, will be ideal for all-sky cosmological studies and presents an exciting new oppor-

tunity for ISW detection.

Appendix A

Full Mathematical Derivations

Here follows a full derivation of the the theoretical prediction of the ISW effect. The first section is a derivation of the auto- and cross-correlation functions, following the doctoral thesis of Francis (2007)*. The second section is the re-expression of the auto- and cross-correlation functions, converting them to equations dependent only on redshift z.

A.1 Angular Power Spectrum of the CMB due to the ISW Effect

Equation 1.1, the equation describing the temperature fluctuations induced along the line of sight, can also be expressed in terms of a unit vector along the line of sight (Cooray & Sheth 2002):

$$T(\hat{\mathbf{n}}) = \frac{\Delta T^{\mathrm{ISW}}}{T_{\mathrm{CMB}}}(\hat{\mathbf{n}}) = 2\int \frac{\dot{\Phi}(\hat{\mathbf{n}}r, r)}{c^3} a(r)\,\mathrm{d}r \tag{A.1}$$

where $\hat{\mathbf{n}}$ is a unit vector along the line of sight, r is the comoving distance along that line of sight, $a(r)$ is the scale factor and Φ is the Newtonian gravitational potential.

The spherical harmonic coefficients are now given by:

*Kindly provided by Prof. J. A. Peacock.

$$
\begin{aligned}
a_{\ell m} &= \int T(\hat{\mathbf{n}}) Y_\ell^{m*}(\hat{\mathbf{n}})\, \mathrm{d}\hat{\mathbf{n}} \\
T^{\mathrm{ISW}}(\hat{\mathbf{n}}) &= 2\int\int \frac{\dot{\Phi}(\mathbf{k})}{c^3} \exp\left(i\mathbf{k}\cdot\hat{\mathbf{n}}r\right) \frac{\mathrm{d}^3\mathbf{k}}{(2\pi)^3}\, a(r)\, \mathrm{d}r \\
\Rightarrow a_{\ell m}^{\mathrm{ISW}} &= \int \left(2\int\int \frac{\dot{\Phi}(\mathbf{k})}{c^3} \exp\left(i\mathbf{k}\cdot\hat{\mathbf{n}}r\right) \frac{\mathrm{d}^3\mathbf{k}}{(2\pi)^3}\, a(r)\, \mathrm{d}r \right) Y_\ell^{m*}(\hat{\mathbf{n}})\, \mathrm{d}\hat{\mathbf{n}} \\
&= \int\int\int 2\frac{\dot{\Phi}(\mathbf{k})}{c^3} \sum_{\ell' m'} 4\pi i^{\ell'} j_{\ell'}(kr) Y_{\ell'}^{m'}(\hat{\mathbf{k}}) Y_{\ell'}^{m'}(\hat{\mathbf{n}}) Y_\ell^{m*}(\hat{\mathbf{n}}) \frac{\mathrm{d}^3\mathbf{k}}{(2\pi)^3}\, a(r)\, \mathrm{d}r \mathrm{d}\hat{\mathbf{n}} \\
&= \sum_{\ell' m'} i^{\ell'} \int \frac{\dot{\Phi}(\mathbf{k})}{c^3} Y_{\ell'}^{m'}(\hat{\mathbf{k}}) \int W^{\mathrm{ISW}}\, j_{\ell'}(kr)\, a(r)\, \mathrm{d}r\, \frac{\mathrm{d}^3\mathbf{k}}{2\pi^2} \int Y_{\ell'}^{m'}(\hat{\mathbf{n}}) Y_\ell^{m*}(\hat{\mathbf{n}})\, \mathrm{d}\hat{\mathbf{n}}
\end{aligned}
$$

where $W^{\mathrm{ISW}} = 2$ and j_ℓ is a spherical Bessel function of the first kind. Since

$$
\int Y_{\ell'}^{m'}(\hat{\mathbf{n}}) Y_\ell^{m*}(\hat{\mathbf{n}})\, \mathrm{d}\hat{\mathbf{n}} = \delta_{\ell\ell'}\delta_{mm'}
$$

the spherical harmonic coefficients can now be expressed as

$$
a_{\ell m}^{\mathrm{ISW}} = i^\ell \int \frac{\dot{\Phi}(\mathbf{k})}{c^3} Y_\ell^m(\hat{\mathbf{k}}) I_\ell(k) \frac{\mathrm{d}^3\mathbf{k}}{2\pi^2}
$$

where $I_\ell = \int W^{\mathrm{ISW}} j_\ell(kr)\, a(r)\, \mathrm{d}r$. The angular power spectrum is then computed as follows:

$$
\begin{aligned}
C_\ell^{\mathrm{ISW}} \delta_{\ell\ell'}\delta_{mm'} &= \langle a_{\ell m} a_{\ell' m'} \rangle \\
&= \left\langle \int \frac{\mathrm{d}^3\mathbf{k}}{2\pi^2} \frac{\dot{\Phi}(\mathbf{k})}{c^3} I_\ell(k) Y_\ell^m(\hat{\mathbf{k}}) \int \frac{\mathrm{d}^3\mathbf{k}'}{2\pi^2} \frac{\dot{\Phi}^*(\mathbf{k}')}{c^3} I_{\ell'}^*(k') Y_{\ell'}^{m'*}(\hat{\mathbf{k}}') \right\rangle \\
&= \int\int \frac{\mathrm{d}^3\mathbf{k}}{2\pi^2} \frac{\mathrm{d}^3\mathbf{k}'}{2\pi^2} \left\langle \frac{\dot{\Phi}(\mathbf{k})}{c^3} \frac{\dot{\Phi}^*(\mathbf{k}')}{c^3} \right\rangle \left\langle Y_\ell^m(\hat{\mathbf{k}}) Y_{\ell'}^{m'*}(\hat{\mathbf{k}}') \right\rangle \langle I_\ell(k) I_{\ell'}^*(k') \rangle \\
&= \int\int \frac{\mathrm{d}^3\mathbf{k}}{2\pi^2} \frac{\mathrm{d}^3\mathbf{k}'}{2\pi^2} \frac{(2\pi)^3}{c^6} \delta_{\mathrm{D}}(\mathbf{k}+\mathbf{k}')\, P_{\dot{\Phi}\dot{\Phi}}(k) \left\langle Y_\ell^m(\hat{\mathbf{k}}) Y_{\ell'}^{m'*}(\hat{\mathbf{k}}') \right\rangle \langle I_\ell(k) I_{\ell'}^*(k') \rangle \\
&= \int \frac{\mathrm{d}^3\mathbf{k}}{\pi} \frac{2}{c^6}\, P_{\dot{\Phi}\dot{\Phi}}(k) \left\langle Y_\ell^m(\hat{\mathbf{k}}) Y_{\ell'}^{m'*}(\hat{\mathbf{k}}) \right\rangle \langle I_\ell(k) I_{\ell'}^*(k) \rangle \\
&= \frac{2}{\pi} \delta_{\ell\ell'}\delta_{mm'} \int \frac{k^2}{c^6}\, P_{\dot{\Phi}\dot{\Phi}}(k)\, |I_\ell(k)|^2\, \mathrm{d}k \\
\Rightarrow C_\ell &= \frac{2}{\pi} \int \frac{k^2}{c^6}\, P_{\dot{\Phi}\dot{\Phi}}(k)\, |I_\ell(k)|^2\, \mathrm{d}k
\end{aligned} \tag{A.2}
$$

In linear theory, $P_{\dot{\Phi}\dot{\Phi}}(k)$ can be expressed as

$$
P_{\dot{\Phi}\dot{\Phi}}(k) = \frac{9}{4} \left(\frac{H_0}{k}\right)^4 \Omega_{m,0}^2 \left(\frac{\mathrm{d}}{\mathrm{d}t} \left[\frac{g}{a} \right] \right)^2 P_{\delta\delta}(k)
$$

so that Equation A.2 can be re-expressed as

$$C_\ell = \frac{18}{\pi}\frac{H_0^4\,\Omega_{m,0}^2}{c^6}\int\frac{\mathrm{d}l}{k^2}\,P_{\delta\delta}(k)\int \mathrm{d}r\;H\;g(f-1)\;j_\ell(kr)\int \mathrm{d}r'\;H\;g(f-1)\;j_\ell(kr')$$

through use of Poisson's equation. In the limit $\ell \to \infty$, we have the Limber approximation

$$j_\ell(x) \to \sqrt{\frac{\pi}{2\ell+1}}\;\delta^K(\ell+1/2-x)$$

and application of this to the expression for C_ℓ gives

$$C_\ell = \frac{9H_0^4\,\Omega_{m,0}^2}{(\ell+1/2)^4\,c^6}\int \mathrm{d}r\;[H\;g(f-1)]^2\;r^2\;P\left(\frac{\ell+1/2}{r}\right) \tag{A.3}$$

which is a very good approximation for $\ell \gtrsim 10$.

A.2 Auto- and Cross-Correlation Predictions

Beginning with Equation 1.9 for the predicted cross-correlation function

$$C_{\mathrm{gT}}(\ell) = -\frac{3\ b\ H_0^2\ \Omega_m\ T}{c^3(\ell+1/2)^2} \int \mathrm{d}r\ \Theta(r)\ H\ (f-1)\ g^2\ P\left(\frac{\ell+1/2}{r}\right)$$

and Equation 1.11 for the predicted auto-correlation function

$$C_{\mathrm{gg}}(\ell) = b^2 \int \mathrm{d}r\ \frac{\Theta^2}{r^2}\ g^2\ P\left(\frac{\ell+1/2}{r}\right)$$

as were described in Section 1.2.

The factor b is the linear galaxy bias as described in Section 1.1, defined by $\delta_{\mathrm{g}} = b\ \delta_{\mathrm{m}}$, where δ_{g} and δ_{m} are the galaxy and matter overdensity fields respectively.

$H_0 \equiv 100h\mathrm{kms}^{-1}\mathrm{Mpc}^{-1}$ is the Hubble constant today.

Ω_m is the matter density parameter today, T is the mean CMB temperature in μK and c is the speed of light in km s^{-1}.

$H(z) \equiv H_0 E(z) = H_0[\Omega_m(1+z)^3 + (1-\Omega_m)]^{1/2}$ is the Hubble parameter, for the flat case where $\Omega_m + \Omega_\Lambda = 1$.

$P = P(k)$ is the power spectrum of matter fluctuations, where k is the Fourier mode in units of h/Mpc. This is obtained from `CAMB` (Lewis et al. 2000),with non-linear corrections performed using `Halofit` (Smith et al. 2003), and for each redshift shell, for the Planck best-fit cosmological parameters (see Table 3.2).

It can be seen that the functions under the integrals contain a mix of parameters that are dependent of both r and z. In order to computationally assess the integrals, for comparison to the observed auto- and cross-correlation functions, these equations need to be rearranged so that they depend only on z.

Recall that $r(z)$ is the comoving distance to redshift z. It is defined as

$$\mathrm{d}r = c\ \frac{\mathrm{d}z}{H(z)}$$

from which follows that

$$r(z) = c \int_0^z \frac{\mathrm{d}x}{H(x)} \tag{A.4}$$

$\Theta(r)$ is the effective radial weight applied to the density field, depending on the redshift distribution in each shell. It is defined as

$$\Theta(r) \equiv \frac{n(r)\, r^2}{\int \mathrm{d}x\; n(x)\, x^2}$$

where $n(r)$ is the background galaxy number density. Since $n(r)$ is expressed in units of $(h/\mathrm{Mpc})^3$, $\Theta(r)$ will have units of h/Mpc.

In order to transform $\Theta(r)$ to redshift dependence, it is necessary to use the projected galaxy overdensity

$$\begin{aligned} \delta_{\mathrm{proj}} &= \int \mathrm{d}r\; \Theta(r)\; \delta(r) \\ &= \int \mathrm{d}z\; \theta(z)\; \delta(z) \end{aligned}$$

where

$$\theta(z) \equiv \frac{\mathcal{N}(z)}{\int \mathrm{d}x\; \mathcal{N}(x)}$$

where $\mathcal{N}(z)$ is the redshift distribution dN/dz in each redshift shell. Note that

$$\theta(z)\; \mathrm{d}z = \Theta(r)\; \mathrm{d}r$$

and $\theta(z)$ is unitless.

Substitution then yields Equation 1.9 as an integral explicitly over z:

$$C_{\mathrm{gT}}(\ell) = -\frac{3\; b\; H_0^3\; \Omega_m\; T}{c^3(\ell + 1/2)^2} \int \mathrm{d}z\; \theta(z)\; E(z)\; (f(z) - 1)\; g(z)^2\; P\left(\frac{\ell + 1/2}{r(z)}\right)$$

The factor of H_0 due to the original $H(z)$ term has been moved outside of the integral, and the factor of h^3 that this brings cancels with the factor of h^{-3} coming from $P(k)$, as $P(k)$ is in units of $(\mathrm{Mpc}/h)^3$.

A similar but somewhat less straightforward approach is taken in the conversion of C_{gg}.

The factor of $\mathrm{d}r \frac{\Theta(r)^2}{r^2}$ is transformed as

$$\begin{aligned} \mathrm{d}r\; \frac{\Theta^2}{r^2} &= \mathrm{d}r\; \Theta(r) \frac{\Theta(r)}{r^2} \\ &= \mathrm{d}z\; \theta(z) \frac{\Theta(r)}{r^2} \end{aligned} \tag{A.5}$$

Then since $\mathrm{d}r = c\; \mathrm{d}z/H(z)$, from Equation A.5 it follows that $\Theta(r) = \theta(z)H(z)/c$. Combining this with $r(z)$ from Equation A.4 gives

$$\begin{aligned} \mathrm{d}r\frac{\Theta^2}{r^2} &= \mathrm{d}z\ \theta(z)\frac{\theta(z)\ H(z)/c}{(c\int_0^z \mathrm{d}x/H(x))^2} \\ &= \mathrm{d}z\ \frac{H_0\ E(z)}{(\int_0^z \mathrm{d}x/(H_0\ E(x)))^2} \\ &= \mathrm{d}z\ \frac{H_0^3}{c^3}\frac{\theta(z)^2 E(z)}{(\int_0^z \mathrm{d}x/E(x))^2} \end{aligned}$$

Substitution of this into Equation 1.11 yields

$$C_{\mathrm{gg}}(\ell) = b^2\frac{H_0^3}{c^3}\int \mathrm{d}z\frac{\theta(z)^2 E(z)}{(\int_0^z \mathrm{d}x/E(x))^2}\ g(z)^2\ P\left(\frac{\ell+1/2}{r(z)}\right) \tag{A.6}$$

for the Limber approximation.

Bibliography

Afshordi, N., Loh, Y.-S., & Strauss, M. A. 2004, Phys. Rev. D, 69, 083524

Alonso, D., Bueno Belloso, A., Sánchez, F. J., García-Bellido, J., & Sánchez, E. 2014, MNRAS, 440, 10

Bilicki, M., Jarrett, T. H., Peacock, J. A., Cluver, M. E., & Steward, L. 2014, ApJS, 210, 9

Boughn, S. & Crittenden, R. 2004, Nature, 427, 45

Boughn, S. P. & Crittenden, R. G. 2002, Physical Review Letters, 88, 021302

Boughn, S. P. & Crittenden, R. G. 2005, Nature, 49, 75

Boughn, S. P., Crittenden, R. G., & Turok, N. G. 1998, New Astron. Rev., 3, 275

Cabré, A., Gaztañaga, E., Manera, M., Fosalba, P., & Castander, F. 2006, MNRAS, 372, L23

Cardelli, J. A., Clayton, G. C., & Mathis, J. S. 1989, ApJ, 345, 245

Cardoso, J.-F., Le Jeune, M., Delabrouille, J., Betoule, M., & Patanchon, G. 2008, IEEE Journal of Selected Topics in Signal Processing, 2, 735

Coles, P. & Jones, B. 1991, MNRAS, 248, 1

Colless, M., Dalton, G., Maddox, S., et al. 2001, MNRAS, 328, 1039

Collister, A. A. & Lahav, O. 2004, PASP, 116, 345

Cooray, A. & Sheth, R. 2002, Phys. Rep., 372, 1

Crittenden, R. G. & Turok, N. 1996, Physical Review Letters, 76, 575

Dekel, A. & Lahav, O. 1999, ApJ, 520, 24

Delabrouille, J., Cardoso, J.-F., Le Jeune, M., et al. 2009, A&A, 493, 835

Eisenstein, D. J., Weinberg, D. H., Agol, E., et al. 2011, AJ, 142, 72

Eriksen, H. K., Dickinson, C., Lawrence, C. R., et al. 2006, ApJ, 641, 665

Fernández-Cobos, R., Vielva, P., Barreiro, R. B., & Martínez-González, E. 2012, MNRAS, 420, 2162

Ferraro, S., Sherwin, B. D., & Spergel, D. N. 2014, ArXiv e-prints 1401.1193

Flender, S., Hotchkiss, S., & Nadathur, S. 2013, JCAP, 2, 13

Fosalba, P. & Gaztañaga, E. 2004, MNRAS, 350, L37

Fosalba, P., Gaztañaga, E., & Castander, F. J. 2003, ApJ, 597, L89

Francis, C. L. 2007, PhD thesis, University of Edinburgh

Francis, C. L. & Peacock, J. A. 2010, MNRAS, 406, 2

Gaztañaga, E., Manera, M., & Multamäki, T. 2006, MNRAS, 365, 171

Giannantonio, T., Crittenden, R., Nichol, R., & Ross, A. J. 2012, MNRAS, 426, 2581

Giannantonio, T., Crittenden, R. G., Nichol, R. C., et al. 2006, Phys. Rev. D, 74, 063520

Giannantonio, T., Scranton, R., Crittenden, R. G., et al. 2008, Phys. Rev. D, 77, 123520

Górski, K. M., Hivon, E., Banday, A. J., et al. 2005, ApJ, 622, 759

Goto, T., Szapudi, I., & Granett, B. R. 2012, MNRAS, 422, L77

Granett, B. R., Neyrinck, M. C., & Szapudi, I. 2008, ApJ, 683, L99

Hambly, N. C., MacGillivray, H. T., Read, M. A., et al. 2001, MNRAS, 326, 1279

Hernández-Monteagudo, C. 2010, A&A, 520, A101

Hernández-Monteagudo, C., Ross, A. J., Cuesta, A., et al. 2014, MNRAS, 438, 1724

Ho, S., Hirata, C., Padmanabhan, N., Seljak, U., & Bahcall, N. 2008, Phys. Rev. D, 78, 043519

Huchra, J. P., Geller, M. J., Clemens, C. M., Tokarz, S. P., & Michel, A. 1996, VizieR Online Data Catalog, 7193, 0

Huchra, J. P., Macri, L. M., Masters, K. L., et al. 2012, ApJS, 199, 26

Ilić, S., Langer, M., & Douspis, M. 2013, A&A, 556, A51

Jarrett, T. 2004, PASA, 21, 396

Jarrett, T. H., Chester, T., Cutri, R., et al. 2000, AJ, 119, 2498

Jeffreys, H. 1961, Theory of Probability (3rd Edition) (New York: Oxford University Press)

Jones, D. H., Saunders, W., Colless, M., et al. 2004, MNRAS, 355, 747

Kaiser, N. 1992, ApJ, 388, 272

Kass, R. E. & Raftery, A. E. 1995, Journal of the American Statistical Association, 90, 773

Kneissl, R., Egger, R., Hasinger, G., Soltan, A. M., & Truemper, J. 1997, A&A, 320, 685

Kovács, A. & Szapudi, I. 2014, ArXiv e-prints 1401.0156

Lewis, A., Challinor, A., & Lasenby, A. 2000, ApJ, 538, 473

López-Corredoira, M., Sylos Labini, F., & Betancort-Rijo, J. 2010, A&A, 513, A3

McEwen, J. D., Vielva, P., Hobson, M. P., Martínez-González, E., & Lasenby, A. N. 2007, MNRAS, 376, 1211

McEwen, J. D., Wiaux, Y., Hobson, M. P., Vandergheynst, P., & Lasenby, A. N. 2008, MNRAS, 384, 1289

Nishizawa, A. J. 2014, Progress of Theoretical and Experimental Physics, 2014, B6110

Nolta, M. R., Wright, E. L., Page, L., et al. 2004, ApJ, 608, 10

Padmanabhan, N., Hirata, C. M., Seljak, U., et al. 2005, Phys. Rev. D, 72, 043525

Pietrobon, D., Balbi, A., & Marinucci, D. 2006, Phys. Rev. D, 74, 043524

Planck Collaboration, Ade, P. A. R., Aghanim, N., et al. 2013a, ArXiv e-prints 1303.5062

Planck Collaboration, Ade, P. A. R., Aghanim, N., et al. 2013b, ArXiv e-prints 1303.5072

Planck Collaboration, Ade, P. A. R., Aghanim, N., et al. 2013c, ArXiv e-prints 1303.5079

Raccanelli, A., Bonaldi, A., Negrello, M., et al. 2008, MNRAS, 386, 2161

Rassat, A., Land, K., Lahav, O., & Abdalla, F. B. 2007, MNRAS, 377, 1085

Sachs, R. K. & Wolfe, A. M. 1967, ApJ, 147, 73

Sawangwit, U., Shanks, T., Cannon, R. D., et al. 2010, MNRAS, 402, 2228

Schechter, P. 1976, ApJ, 203, 297

Schlegel, D. J., Finkbeiner, D. P., & Davis, M. 1998, ApJ, 500, 525

Scranton, R., Connolly, A. J., Nichol, R. C., et al. 2003, ArXiv e-prints 0307.0335

Smith, R. E., Peacock, J. A., Jenkins, A., et al. 2003, MNRAS, 341, 1311

Vielva, P., Martínez-González, E., & Tucci, M. 2006, MNRAS, 365, 891

Wright, E. L., Eisenhardt, P. R. M., Mainzer, A. K., et al. 2010, AJ, 140, 1868

Xia, J.-Q., Viel, M., Baccigalupi, C., & Matarrese, S. 2009, JCAP, 9, 3